SYSTEMATIC NON-LTE STUDY OF THE −2.6 ⩽ [Fe/H] ⩽ 0.2 F AND G DWARFS IN THE SOLAR NEIGHBORHOOD. II. ABUNDANCE PATTERNS FROM Li TO Eu[*]

G. Zhao[1,2], L. Mashonkina[3], H. L. Yan[1], S. Alexeeva[3], C. Kobayashi[4], Yu. Pakhomov[3], J. R. Shi[1,2], T. Sitnova[3], K. F. Tan[1], H. W. Zhang[5,6], J. B. Zhang[1,2], Z. M. Zhou[1,2], M. Bolte[7], Y. Q. Chen[1], X. Li[1], F. Liu[1,8], and M. Zhai[1]

[1] Key Laboratory of Optical Astronomy, National Astronomical Observatories, Chinese Academy of Sciences, Beijing 100012, China; gzhao@nao.cas.cn
[2] School of Astronomy and Space Science, University of Chinese Academy of Sciences, Beijing 100049, China
[3] Institute of Astronomy, Russian Academy of Sciences, RU-119017 Moscow, Russia; lima@inasan.ru
[4] School of Physics, Astronomy and Mathematics, Centre for Astrophysics Research, University of Hertfordshire, College Lane, Hatfield AL10 9AB, UK
[5] Department of Astronomy, School of Physics, Peking University, Beijing 100871, China
[6] Kavli Institute for Astronomy and Astrophysics, Peking University, Beijing 100871, China
[7] UCO/Lick Observatory, University of California, 1156 High Street, Santa Cruz, CA 95064, USA
[8] Research School of Astronomy and Astrophysics, Australian National University, Canberra, ACT 2611, Australia
Received 2016 July 1; revised 2016 September 16; accepted 2016 September 27; published 2016 December 19

ABSTRACT

For the first time, we present an extensive study of stars with individual non-LTE (NLTE) abundances for 17 chemical elements from Li to Eu in a sample of stars uniformly distributed over the $-2.62 \leqslant$ [Fe/H] $\leqslant +0.24$ metallicity range that is suitable for the Galactic chemical evolution research. The star sample has been kinematically selected to trace the Galactic thin and thick disks and halo. We find new results and improve earlier ones as follows: (i) the element-to-iron ratios for Mg, Si, Ca, and Ti form a metal-poor (MP) plateau at a similar height of 0.3 dex, and the knee occurs at common [Fe/H] $\simeq -0.8$. The knee at the same metallicity is observed for [O/Fe], and the MP plateau is formed at [O/Fe] = 0.61. (ii) The upward trend of [C/O] with decreasing metallicity exists at [Fe/H] < −1.2, supporting the earlier finding of Akerman et al. (iii) An underabundance of Na relative to Mg in the [Fe/H] < −1 stars is nearly constant, with the mean [Na/ Mg] $\simeq -0.5$. (iv) The K/Sc, Ca/Sc, and Ti/Sc ratios form well-defined trends, suggesting a common site of the K–Ti production. (v) Sr follows the Fe abundance down to [Fe/H] $\simeq -2.5$, while Zr is enhanced in MP stars. (vi) The comparisons of our results with some widely used Galactic evolution models are given. The use of the NLTE element abundances gives increased credit to the interpretation of the data in the context of the chemical evolution of the Galaxy.

Key words: Galaxy: evolution – line: formation – stars: abundances – stars: atmospheres – stars: late-type

Supporting material: machine-readable table

1. INTRODUCTION

The understanding of the formation and evolution of the Galaxy mainly relies on the stellar spectroscopic analysis, which gives the chemical compositions of unevolved cool stars. Pioneering studies in this field (e.g., Wallerstein 1962; Zhao & Magain 1990a, 1990b) have found that $[\alpha/\mathrm{Fe}]$[9] versus [Fe/H] shows a plateau below [Fe/H] = −1, and then there is a steady decline to $[\alpha/\mathrm{Fe}] \sim 0$ at the solar metallicity, which is actually a composite of the ratios transiting from the halo to the thick- and thin-disk populations. That is, the "chemical tagging" can be used to recover the star formation and evolution history of the Galaxy. However, they are found to span a large range in the overall abundance, of more than 8 orders of magnitude. Stellar abundance trends establish important observational constraints on current models of nucleosynthesis and the chemical evolution of the Galaxy (e.g., Spite & Spite 1978; McWilliam et al. 1995; Cayrel et al. 2004; Kobayashi et al. 2006; Bensby et al. 2014).

In order to interpret these abundance ratios, the chemical evolution model is introduced to help in understanding some basic qualitative concepts. The general trends of observational abundances of stars can be readily explained by the simple model of Galactic chemical evolution (hereafter GCE) with

outflow, as suggested by Timmes et al. (1995). However, a number of new results have put more complex constraints on the physical scenarios of the Galaxy. In particular, the building of the Galactic halo in the framework of hierarchical galaxy formation and the significant role of radial migration in the Galactic disk should be properly considered in the GCE models. Several attempts to account for these processes have been undertaken in the past years through numerical simulations (e.g., Salvadori et al. 2007; Roškar et al. 2008).

The majority of current chemical evolution models are based on high-resolution observations of stars in the solar neighborhood. However, the fractions of population measured in the solar vicinity are not representative enough for the entire Galaxy. In particular, the outer halo of the Galaxy may be dominated by the merging imprints of nearby dwarf galaxies, where the chemical evolution proceeds at a lower rate than that of the inner region of the Galaxy. Moreover, even for stars in the solar neighborhood, they have distinct abundance distributions (see, e.g., Nissen & Schuster 1997, 2010), indicating the complex chemical evolution of the Galaxy at different locations. To decipher the spectral fingerprints in terms of abundances requires realistic models for the stellar atmospheres and the line-formation processes. Still today, the vast majority of abundance analysis of late-type stars relies on the assumption of local thermodynamic equilibrium (LTE). It is expected that this approach quite often gives misleading results, and for many elements such systematic errors may be very severe (see Figure 7 of Gehren et al. 2006, as an example). The

---

[*] Based on observations collected at the UCO/Lick Observatory, USA, and the Canada–France–Hawaii Telescope.
[9] In the classical notation, where $[\mathrm{X/H}] = \log{(N_\mathrm{X}/N_\mathrm{H})_\mathrm{star}} - \log{(N_\mathrm{X}/N_\mathrm{H})_\mathrm{Sun}}$.

principles of non-LTE (NLTE) line formation and codes capable of such calculations have been around for a long time but have only been explored in a more systematic fashion for a wide range of stellar parameters over the past decade or so (e.g., Zhao et al. 1998; Zhao & Gehren 2000; Mashonkina & Gehren 2001; Takeda et al. 2002; Gehren et al. 2004; Fabbian et al. 2006; Mashonkina & Zhao 2006; Zhang et al. 2006b; Mashonkina et al. 2007a, 2008; Bergemann & Gehren 2008; Zhang et al. 2008; Lind et al. 2009; Shi et al. 2009; Andrievsky et al. 2010; Bergemann et al. 2010; Bergemann & Cescutti 2010; Spite et al. 2011, 2012; Yan et al. 2015).

Before the observations are used to give constraints to the GCE models, we need to take into account the analysis errors of the stellar abundances, such as the departures from LTE and uncertainties in the atmospheric parameters. In particular, most high-resolution spectroscopic studies are based on the LTE assumption, which may not be valid for spectral lines. It is suspected that both the unexpected behavior of the scatter of the abundance ratios and the different behavior between dwarfs and giants found in the LTE studies could be due at least partly to the neglect of the departures from LTE (Andrievsky et al. 2010). Actually, NLTE analysis is important in the sense that it can improve the accuracy of stellar abundances, while LTE can achieve a very high precision with a large systematic deviation. In order to link the observations of abundance ratios with GCE models, we need more accuracy than precision. In particular, a modeling technique allowing for departures from LTE can be used to accurately predict iron abundances and spectroscopic stellar parameters for a set of benchmark late-type stars.

The $[\alpha/\mathrm{Fe}]$ ratios can be more accurately derived by performing the NLTE analysis of both α-elements (Mg, Si, Ca, Ti) and iron abundances. It is well known that $[\mathrm{O}/\mathrm{Fe}]$ and $[\alpha/\mathrm{Fe}]$ ratios are the most important indicators for distinguishing different chemical enrichment histories among the populations in the Galaxy or between the Galaxy and nearby dwarf galaxies. For various chemical species, a change of the element abundance during the Galactic evolution may consist of only a few tenths of one magnitude. To make stellar abundance trends visible if they exist, one needs to determine the differential abundances with the accuracy of 0.1 dex or better.

A systematic NLTE abundance analysis of F and G dwarfs and subgiants seems worthwhile and timely. These stars are still the most commonly used beacons for studies of Galactic chemical evolution due to their sheer numbers and long lifetimes. An additional reason for limiting the discussions to F and G dwarfs is that these should be similar to the Sun, which can therefore be used as a test bench of the modeling. However, due to the increasing numerical complexity, compared with the LTE case, NLTE investigations have previously been limited to individual stars and usually only a handful of spectral lines. Contrary to the vast majority of abundance analyses available in the literature (e.g., Prochaska et al. 2000; Mishenina & Kovtyukh 2001; Reddy et al. 2003; Allende Prieto et al. 2004; Ishigaki et al. 2013), the present study will be based on NLTE line formation for Li I, C I, O I, Na I, Mg I, Al I, Si I–Si II, K I, Ca I, Sc II, Ti II, Fe I–Fe II, Cu I, Sr II, Zr II, Ba II, and Eu II. For each listed species, the original model atom was treated and tested by our previous studies (see Table 1 for details). The wavelength range is selected so that the lines of the NLTE elements are presented in the spectral coverage.

Table 1
Atomic Models Used in This Study and Treatment of A + H I Inelastic Collisions

Species	Model Atom	A + H I
Li I	Shi et al. (2007)	BB03
C I	Alexeeva & Mashonkina (2015)	$S_{\mathrm{H}}^{\mathrm{a}} = 0.3$
O I	Sitnova et al. (2013)	$S_{\mathrm{H}} = 1.0$
Na I	Gehren et al. (2004)	$S_{\mathrm{H}} = 0.05$
Mg I	Mashonkina (2013)	BB12
Al I	Baumueller & Gehren (1996)	B13
Si I–Si II	Shi et al. (2008)	BYB14
K I	Zhang et al. (2006a)	$S_{\mathrm{H}} = 0.05$
Ca I	Mashonkina et al. (2007a)	$S_{\mathrm{H}} = 0.1$
Sc II	Zhang et al. (2008)	$S_{\mathrm{H}} = 0.1$
Ti II	Sitnova et al. (2016)	$S_{\mathrm{H}} = 1.0$
Fe I–Fe II	Mashonkina et al. (2011)	$S_{\mathrm{H}} = 0.5$
Cu I	Shi et al. (2014)	$S_{\mathrm{H}} = 0.1$
Sr II	Mashonkina & Gehren (2001)	$S_{\mathrm{H}} = 0.01$
Zr II	Velichko et al. (2010)	$S_{\mathrm{H}} = 1.0$
Ba II	Mashonkina et al. (1999)	$S_{\mathrm{H}} = 0.01$
Eu II	Mashonkina & Gehren (2000)	$S_{\mathrm{H}} = 0.1$

Notes. BB03—Belyaev & Barklem (2003); BB12—Barklem et al. (2012); B13 —Belyaev (2013); BYB14—Belyaev et al. (2014).
[a] Scaling factor to the Darwinian rates.

In this work, we aim to define a large sample, the F and G benchmark stars, which include 51 F and G dwarfs and subgiants in a limited range of temperatures, gravities, and metallicities. These stars should be representative of the different stellar populations of the Galaxy. Most of these stars were studied under the LTE assumption in the past years. Their accurate stellar parameters have been determined carefully by Sitnova et al. (2015, hereafter Paper I). It is important to have new abundances derived from the NLTE analysis, which will better constrain the models of the Galactic chemical evolution and the yields of supernovae (SNe; e.g., Matteucci & Francois 1989; Woosley & Weaver 1995; Thielemann et al. 1996; Nomoto et al. 2006).

In this paper, Section 2 describes the stellar sample, observations, and atmospheric parameters. Details of the NLTE calculations, including the atomic models and mechanisms of the departures from LTE, are given in Section 3. Section 4 presents the abundance results for the sample stars. In Section 5 we discuss the implications for the GCE model and nucleosynthesis, followed by a short section of conclusions.

2. STELLAR SAMPLE, OBSERVATIONS, AND ATMOSPHERIC PARAMETERS

Our stellar sample, the observed stellar spectra, and the determination of atmospheric parameters were presented in Paper I. Here, we review the main points and describe briefly a reduction of the infrared (IR) spectra undertaken to remove fringes in the echelle orders, where the O I $\lambda\lambda7771-5$ triplet lines are located.

The sample includes 51 nearby stars uniformly distributed in the $-2.62 \leqslant [\mathrm{Fe}/\mathrm{H}] \leqslant +0.24$ metallicity range. We selected unevolved stars, i.e., mostly dwarfs, with a few subgiants added. The Galactic thin-disk stellar population is well represented in our sample by 27 stars, with $[\mathrm{Fe}/\mathrm{H}]$ down to -0.78. We have eight thick-disk stars in the $-1.47 \leqslant [\mathrm{Fe}/\mathrm{H}] \leqslant -0.70$ range, overlapping only a little with that of the thin-disk and 16 halo stars. Membership of individual stars in

the galactic stellar populations was identified based mainly on the star's kinematics.

Observations. Spectra of 48 stars were obtained for our project using the Hamilton Echelle Spectrograph mounted on the Shane 3 m telescope of the Lick Observatory. Their resolving power is $R = \lambda/\Delta\lambda \simeq 60,000$, the spectral coverage is 3700–9300 Å, and the signal-to-noise ratio (S/N) at 5500 Å is higher than 100 for most stars. For two stars their spectra were obtained with CFHT/ESPaDOnS, as described in Paper I. The high-quality observed spectrum of HD 140283 was taken from the ESO UVESPOP survey (Bagnulo et al. 2003). For some stars our observational material was complemented with the data from our earlier projects, namely, VLT2/UVES, 67.D-0086A (HD 74000, BD −04°3208), and 2.2 m/FOCES (HD 59374, HD 59984, HD 103095, HD 134169). We also employed the archives of CFHT/ESPaDOnS[10] for BD −13° 3442, VLT2/UVES, and 3.6 m/HARPS[11] for HD 59374 (074. C-0364(A), $R \simeq 115,000$), HD 59984 (076.B-0133(A), $R \simeq 57,000$), HD 100563 ($R \simeq 115,000$), and HD 108177 ($R \simeq 115,000$), as well as 1.93 m/SOPHIE[12] ($R = 76,500$) and 1.93 m/ELODIE[13] ($R = 42,000$) for HD 64090 and BD +66°0268.

Fringe reduction. The O I $\lambda\lambda7771-5$ lines are located in the two overlapping echelle orders, 97th and 98th, of the Hamilton spectrograph (Figures 1(a) and (b)). We propose the following procedure to remove the fringing effects. The intensity of CCD fringes depends on the wavelength and the thickness of a silicon layer of CCD. Although the standard flat fielding could be used to remove fringes, this procedure is limited by the bright scattered light. Here we apply a statistical procedure based on a set of stellar spectra with similar exposures taken on one night. We show below that due to a comparable level of the scattered light in stellar spectra, the fringes can be recovered with a reasonable precision. Moreover, different stellar radial velocities provide us with the possibility to recover the fringes even in the continuum around absorption lines. Obviously, the accuracy of this statistical procedure depends on the spectra sample volume.

The statistical approach was applied on each night to fit the fringes in the vicinity of oxygen lines. For the observational set in 2011 March we used seven working stars, while we used 14−19 working stars for the 2012 observations. The processing starts from raw CCD images with subtracted bias. For each star we find positions of echelle orders and the light distribution along the slit. We then extracted 11 spectra of 1 pixel height along the slit and processed them independently. The sixth spectrum corresponding to the slit center is shown in Figures 1(a) and (b). All stellar and telluric lines were removed in order to use only the continuum spectrum. We select the star with the spectrum $I_0(\lambda)$ of the highest S/N and reduce spectra $I_*(\lambda)$ of other working stars to the selected spectrum using the relation $I'_*(\lambda) = S(\lambda)I_*(\lambda)$, where $S(\lambda)$ is the smooth spline approximation of the function $I_0(\lambda)/I_*(\lambda)$.

The median averaging of the $I'_*(\lambda)$ spectra of all working stars gives us 11 spectra of the fringes along the slit, which are then used to normalize the stellar spectra. Eleven normalized spectra for each star were averaged with weights depending on the light distribution along the slit. This procedure was applied

---

[10] http://www.cadc-ccda.hia-iha.nrc-cnrc.gc.ca/en/search/
[11] http://archive.eso.org/wdb/wdb/adp/phase3-main/query
[12] http://atlas.obs-hp.fr/sophie/
[13] http://atlas.obs-hp.fr/elodie/
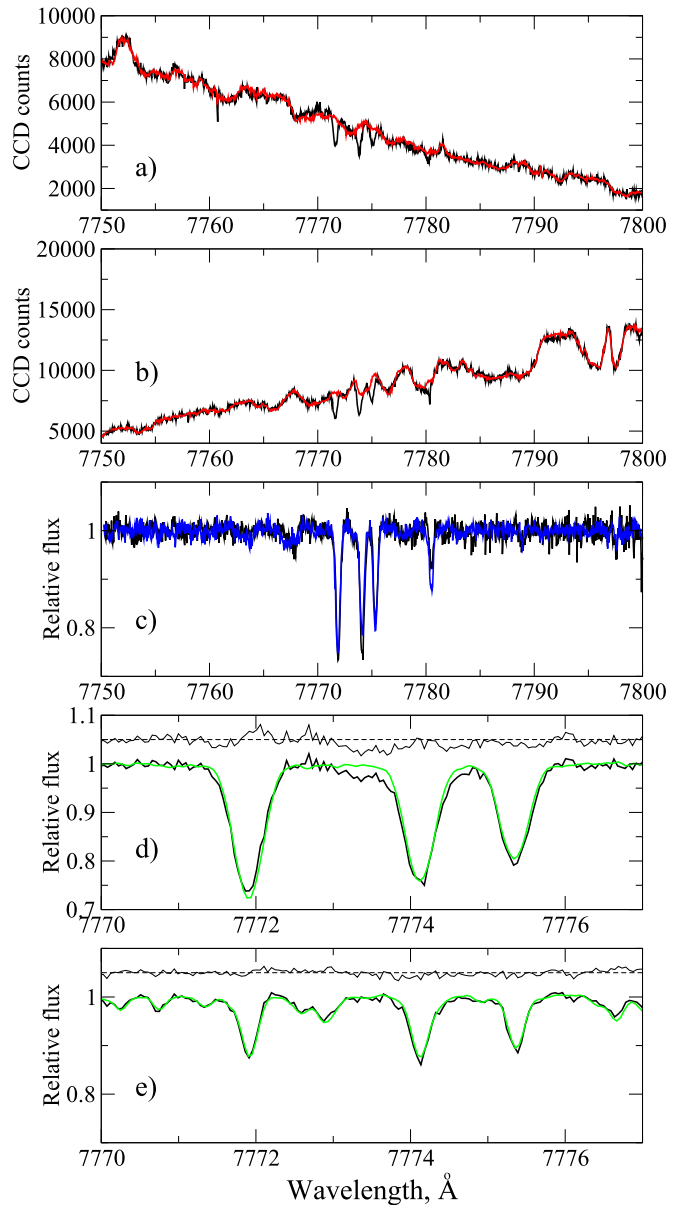
Figure 1. Fringe reduction in the HD 49933 and HD 142091 spectra. (a) Fragment of the HD 49933 spectrum from the slit center of the 97th echelle order (black curve) and the recovered fringes for the same position on the slit (red curve). (b) Same as in panel (a), but for the overlapping part of the 98th echelle order. (c) Reduced and normalized spectra of the 97th (black curve) and 98th (blue curve) echelle orders. (d) Reduced Hamilton (black curve) and the ESPaDOnS (green curve) spectrum of HD 49933. The difference between the two spectra is shown in the upper part of the panel. (e) Same as in panel (d), but for HD 142091.

to the second overlapping order as well. The reduced spectra are shown in Figure 1(c). Both spectra were then averaged with weights depending on their CCD signal level. A precise wavelength calibration is required to correctly perform the spectral averaging. We used a wavelength solution of the Ta–Th–Ar hollow cathode lamp (Pakhomov 2015) for the observations taken in 2011 March and the Ti–Ar lamp (Pakhomov & Zhao 2013) for the observations of 2012.

In Figures 1(d) and (e) we compare spectra of HD 49933 and HD 142091 observed with the Hamilton spectrograph ($R = 60,000$) and reduced in this study with the corresponding ESPaDOnS spectra, which are free of fringes. It is worth noting

that the latter $R = 80,000$ and S/N > 200 spectra were degraded to $R = 60,000$. In the case of HD 49933 the rms of the difference between the Hamilton and ESPaDOnS spectra amounts to 0.0114, which corresponds to S/N = 90, slightly lower than the S/N = 110 of the original IR spectrum of this star. In the case of HD 142091 the rms value is 0.0059 (S/N = 170 versus the original S/N = 250). Thus, the statistical approach is efficient in removing the fringes.

Stellar atmosphere parameters. A combination of the photometric and spectroscopic methods was applied to derive a homogeneous set of the stellar atmosphere parameters: effective temperature $T_{\rm eff}$, surface gravity $\log g$, [Fe/H], and microturbulence velocity ξ_t. Our spectroscopic analyses took advantage of employing the NLTE line formation for Fe I–Fe II. Paper I estimated the systematic and statistical errors of $T_{\rm eff}$ to be 50 and 70 K, respectively, the uncertainty in $\log g/\xi_t$ to be 0.04 dex/0.14 km s^{-1}, and the statistical error of [Fe/H] was defined by the dispersion, σ, for lines of Fe II in a given star. For most stars the latter value amounts to 0.03−0.09 dex. Hereafter, the statistical abundance error is the dispersion in the single line measurements about the mean: $\sigma = \sqrt{\Sigma(x - x_i)^2/(N - 1)}$.

Our sample of unevolved stars, which are uniformly distributed in a wide metallicity range, belong to the three different Galactic stellar populations and have accurate and homogeneous atmospheric parameters suitable for Galactic chemical evolution studies.

3. NLTE CALCULATIONS

3.1. NLTE Methods

Our present investigation is based on the NLTE methods treated in our earlier studies and documented in a number of papers, where atomic data and the problems of line formation have been considered in detail. Table 1 lists the investigated chemical species and cites the related papers. Compared with the published model atoms, collisional data were updated for several chemical species. For Ca II and Sr II we apply here electron-impact excitation rate coefficients from ab initio calculations of Meléndez et al. (2007) and Bautista et al. (2002), respectively. For Li I, Mg I, Al I, and Si I inelastic collisions with neutral hydrogen particles are treated using accurate rate coefficients from quantum mechanical calculations of Belyaev & Barklem (2003), Barklem et al. (2012), Belyaev (2013), and Belyaev et al. (2014), respectively. For the remaining species hydrogen collisions are computed using the formula of Steenbock & Holweger (1984) with a scaling factor $S_{\rm H}$ estimated empirically in the literature from their different influence on the different lines of a given atom in solar and stellar spectra. The references and recommended $S_{\rm H}$ values are indicated in Table 1.

In order to solve the coupled radiative transfer and statistical equilibrium equations for metals, we use a revised version of the DETAIL program (Butler & Giddings 1985) based on the accelerated lambda iteration, which follows the efficient method described by Rybicki & Hummer (1991, 1992). The update was presented by Mashonkina et al. (2011). The obtained departure coefficients were then used by the codes SIU (Reetz 1991) and SYNTHV-NLTE (Ryabchikova et al. 2016) to calculate the synthetic line profiles.

As in Paper I, in this study we used the MARCS model structures (Gustafsson et al. 2008).

3.2. Line List and Solar Abundances for a Differential Analysis

The lines used in the abundance analysis were selected from the lists of our NLTE papers (see Table 1 for references). They are listed in Table 2 along with the adopted atomic parameters.

The van der Waals damping was computed following the perturbation theory, where the data were available, using the van der Waals damping constants $\Gamma_6/N_{\rm H}$ at 10,000 K as provided by Barklem et al. (2000). An exception was the selected lines of some elements, for which we used the C_6-values derived from solar line-profile fitting. If no other data were available, the $\Gamma_6/N_{\rm H}$ values from Kurucz's calculations[14] were employed.

Some elements considered here are represented by either a single isotope with an odd number of nucleons (Sc) or multiple isotopes with measured wavelength differences ($\Delta\lambda \geqslant 0.01$ Å for Li I, Cu I, Sc II, Ba II, and Eu II). Nucleon−electron spin interactions in odd-A isotopes lead to hyperfine splitting of the energy levels, resulting in absorption lines divided into multiple components. Without accounting properly for hyperfine structure (HFS) and/or isotopic structure (IS), abundances determined from the lines sensitive to these effects can be severely overestimated.

HFS and IS are taken into account when necessary with the data from Sansonetti et al. (1995, Li I), Zhang et al. (2008, Sc II), Shi et al. (2014, Cu I), Borghs et al. (1983, Sr II), Robert Kurucz's Web site (http://kurucz.harvard.edu/atoms.html, Ba II), and Lawler et al. (2001, Eu II). For Li, Cu, Sr, Ba, and Eu, we use the fractional isotope abundances corresponding to the solar system matter (Lodders et al. 2009, pp. 44–54).

The Sun is used as a reference star for a subsequent stellar abundance analysis. The solar flux observations were taken from the Kitt Peak Solar Atlas (Kurucz et al. 1984). The calculations were performed with the MARCS model atmosphere 5777/4.44/0 (Gustafsson et al. 2008). A depth-independent microturbulence of 0.9 km s^{-1} was adopted. Our synthetic flux profiles were convolved with a profile that combines a rotational broadening of 1.8 km s^{-1} and broadening by macroturbulence with a radial-tangential profile. The $V_{\rm mac}$ values varied mainly between 2.6 and 3.3 km s^{-1} for the strong lines and between 3.4 and 4.0 km s^{-1} for the weak lines. For comparison, Gray (1977) found solar macroturbulence velocities varying between 2.9 and 3.8 km s^{-1} for a small sample of the solar Fe I lines. Solar LTE and NLTE abundances from the individual lines are presented in Table 2.

3.3. Departures from LTE for Individual Spectral Lines

Our calculations show that the departures from LTE are different for lines of different chemical species and different for lines of any given species. For each individual line the NLTE effects depend on stellar parameters. Figure 2 displays the NLTE abundance corrections, $\Delta_{\rm NLTE} = \log \varepsilon_{\rm NLTE} - \log \varepsilon_{\rm LTE}$, for the representative lines of different species in our stellar sample, and Figure 3 illustrates the departures from LTE in the line profiles. All the investigated NLTE species can be separated into five groups depending on the dominant NLTE mechanism.

1. *The photoionization-dominated minority species Mg I, Al I, Si I, Ca I, Ti I, Fe I, and Cu I.* Departures from LTE for these species are mainly caused by superthermal radiation of

---

[14] http://kurucz.harvard.edu/atoms.html

Table 2
Line Data, References to Their Sources, and the Obtained Solar Element LTE and NLTE Abundances, $\log \varepsilon_\odot$

λ, Å	E_{exc} (eV)	log gf	Ref.	log C_6	Ref.	$\log \varepsilon_\odot$ LTE	$\log \varepsilon_\odot$ NLTE	λ, Å	E_{exc} (eV)	log gf	Ref.	log C_6	Ref.	$\log \varepsilon_\odot$ LTE	$\log \varepsilon_\odot$ NLTE
Li I								Ca I							
6707.80[a]	0.00	0.17	NIST	−31.22	ABO			5512.98	2.93	−0.46	S88	−30.61	S81	6.45	6.42
								5588.75	2.53	0.36	SR81	−31.39	S81	6.35	6.29
C I								5590.12	2.51	−0.57	SR81	−31.39	S81	6.45	6.37
4932.05	7.68	−1.66	NIST	−30.50	K12	8.48	8.45	5857.45	2.93	0.24	SR81	−30.61	S81	6.42	6.38
5052.14	7.68	−1.30	NIST	−30.60	K12	8.49	8.46	5867.57	2.93	−1.57	S88	−30.97	K07	6.36	6.38
5380.33	7.68	−1.62	NIST	−30.75	K12	8.46	8.43	6161.29	2.51	−1.27	SR81	−30.48	S81	6.36	6.36
6587.61	8.54	−1.00	NIST	−30.47	K12	8.45	8.43	6162.17	1.90	−0.09	SN75	−30.30	ABO	6.29	6.26
8335.15	7.68	−0.44	NIST	−30.53	ABO	8.54	8.43	6166.44	2.51	−1.14	SR81	−30.48	S81	6.41	6.40
9061.43	7.48	−0.35	NIST	−30.72	ABO	8.68	8.43	6169.06	2.51	−0.80	SR81	−30.48	S81	6.45	6.41
9062.47	7.48	−0.46	NIST	−30.72	ABO	8.68	8.43	6169.56	2.53	−0.48	SR81	−30.48	S81	6.45	6.41
9078.29	7.48	−0.58	NIST	−30.72	ABO	8.65	8.46	6439.08	2.53	0.39	SR81	−31.58	S81	6.30	6.13
9088.51	7.48	−0.43	NIST	−30.72	ABO	8.68	8.43	6449.81	2.52	−0.50	SR81	−31.45	S81	6.46	6.26
9094.83	7.49	0.15	NIST	−30.72	ABO	8.72	8.40	6455.60	2.51	−1.34	SR81	−31.45	S81	6.39	6.33
9111.81	7.49	−0.30	NIST	−30.72	ABO	8.67	8.40	6471.66	2.51	−0.69	SR81	−31.58	S81	6.43	6.26
9405.72	7.68	0.29	NIST	−30.62	ABO	8.79	8.40	6493.78	2.52	−0.11	SR81	−31.58	S81	6.43	6.24
								6499.65	2.51	−0.82	SR81	−31.58	S81	6.43	6.29
O I															
6158.15	10.74	−1.84	NIST	−29.47		8.84	8.82	Sc II							
6158.18	10.74	−1.00	NIST	−29.47		8.84	8.82	4670.40[b]	1.35	−0.58	LD89	−32.00	ZGZ	3.07	3.03
6158.19	10.74	−0.41	NIST	−29.47		8.84	8.82	5031.02[b]	1.35	−0.40	LD89	−32.08	ZGZ	3.09	3.06
7771.94	9.15	0.37	NIST	−30.99		8.92	8.74	5526.81[b]	1.76	−2.11	LD89	−32.07	ZGZ	3.16	3.08
7774.16	9.15	0.22	NIST	−30.99		8.91	8.75	5640.97[b]	1.49	−1.13	LD89	−32.15	ZGZ	3.07	3.05
7775.39	9.15	0.00	NIST	−30.99		8.89	8.75	5657.87[b]	1.50	−0.60	LD89	−32.15	ZGZ	3.17	3.09
								5667.16[b]	1.49	−1.31	LD89	−32.15	ZGZ	3.12	3.11
Na I								5669.03[b]	1.49	−1.20	LD89	−32.15	ZGZ	3.10	3.09
5682.64	2.10	−0.71	NIST	−29.78	Sun	6.36	6.28	5684.19[b]	1.50	−1.07	LD89	−32.15	ZGZ	3.11	3.09
5688.21	2.10	−0.41	NIST	−29.78	Sun	6.35	6.26	6245.63[b]	1.50	−1.03	K12	−32.06	ZGZ	3.02	3.00
5889.96	0.00	0.11	NIST	−31.60	Sun	6.32	6.31								
5895.93	0.00	−0.19	NIST	−31.60	Sun	6.32	6.31	Ti II							
6154.23	2.10	−1.55	NIST	−30.05	Sun	6.30	6.27	4395.84	1.24	−1.93	WLS			4.98	4.98
6160.75	2.10	−1.25	NIST	−30.05	Sun	6.33	6.28	4464.45	1.16	−1.81	WLS			5.09	5.08
								4470.85	1.16	−2.02	WLS			4.97	4.96
Mg I								4488.32	3.12	−0.50	WLS			4.98	4.98
4571.09	0.00	−5.47	GLS	−31.96	Sun	7.49	7.53	4493.51	1.08	−2.78	WLS			4.88	4.88
4702.99	4.34	−0.38	GLS	−29.71	Sun	7.49	7.50	4583.41	1.16	−2.84	WLS			4.99	4.99
4730.03	4.34	−2.20	GLS	−29.89	Sun	7.51	7.53	4657.20	1.24	−2.29	WLS			4.96	4.96
5528.41	4.34	−0.47	GLS	−30.20	Sun	7.49	7.50	4708.66	1.24	−2.35	WLS			4.99	4.99
5711.07	4.34	−1.64	GLS	−29.89	Sun	7.48	7.50	5005.16	1.57	−2.73	WLS			5.04	5.04
								5185.90	1.89	−1.41	WLS			4.99	4.98
Al I								5211.53	2.59	−1.41	WLS			4.91	4.91
3961.52	0.01	−0.33	NIST	−31.20	Sun	6.31	6.36	5268.62	2.60	−1.61	WLS			4.98	4.98
6696.03	3.14	−1.51	BG96	−30.60	Sun	6.40	6.42	5336.79	1.58	−1.60	WLS			5.01	5.00
6698.67	3.14	−1.87	BG96	−30.60	Sun	6.39	6.41	5381.02	1.57	−1.97	WLS			5.00	5.00
7835.31	4.02	−0.65	K75	−29.77	K12	6.38	6.39	5396.25	1.58	−3.18	WLS			5.02	5.02
7836.13	4.02	−0.49	K75	−29.77	K12	6.37	6.38	5418.77	1.58	−2.13	WLS			4.99	4.99
8772.86	4.02	−0.32	K75	−29.01	ABO	6.37	6.38								
8773.90	4.02	−0.14	K75	−29.01	ABO	6.35	6.36	Cu I							
								5105.54[c]	1.39	−1.52	B75	−31.47	ABO	4.15	4.17
Si I								5218.20[c]	3.82	0.48	B75	−30.37	ABO	4.06	4.06
3905.52	1.91	−1.10	SGM	−30.92	ABO	7.50	7.48	5782.13[c]	1.64	−1.72	B75	−31.46	ABO	4.05	4.08
4102.94	1.91	−2.99	SGM	−30.97	ABO	7.50	7.50								
5690.42	4.71	−1.74	SGM	−30.09	ABO	7.48	7.48	Sr II							
5701.10	4.71	−1.96	SGM	−30.09	ABO	7.45	7.45	4077.72[d]	0.00	0.15	RCW	−31.80	MZG	2.91	2.91
5772.15	5.08	−1.62	SGM	−30.09	ABO	7.50	7.49	4161.79	2.94	−0.50	RCW	−32.00		3.01	3.04
6142.48	5.62	−1.48	SGM	−29.67	ABO	7.53	7.53	4215.54[d]	0.00	−0.17	RCW	−31.80	MZG	2.91	2.91
6145.02	5.62	−1.39	SGM	−29.67	ABO	7.52	7.52								
6155.13	5.62	−0.78	SGM	−29.67	ABO	7.52	7.51	Zr II							
6237.32	5.61	−1.08	SGM	−29.67	ABO	7.52	7.51	4161.21	0.71	−0.59	LNA	−32.00		2.49	2.51
6243.81	5.62	−1.29	SGM	−29.67	ABO	7.53	7.53	4208.98	0.71	−0.51	LNA	−32.00		2.57	2.58
6244.47	5.62	−1.29	SGM	−29.67	ABO	7.54	7.54	5112.27	1.67	−0.85	LNA	−32.00		2.70	2.71

Table 2
(Continued)

λ, Å	$E_{\rm exc}$ (eV)	log gf	Ref.	log C_6	Ref.	log $\varepsilon_\odot$ LTE	log $\varepsilon_\odot$ NLTE	λ, Å	$E_{\rm exc}$ (eV)	log gf	Ref.	log C_6	Ref.	log $\varepsilon_\odot$ LTE	log $\varepsilon_\odot$ NLTE
Si II								Ba II							
6347.11	8.12	0.26	SGM	−30.00		7.50	7.46	4554.03[e]	0.00	0.17	RCW	−31.65	MZG	2.25	2.24
6371.37	8.12	−0.06	SGM	−30.00		7.51	7.49	4934.07[e]	0.00	−0.15	RCW	−31.65	MZG	2.23	2.16
								5853.67	0.60	−1.00	RCW	−31.28	BM98	2.32	2.23
K I								6141.71	0.70	−0.08	RCW	−31.28	BM98	2.29	2.14
7698.98	0.00	−0.18	B00	−31.00	Sun	5.43	5.14	6496.90	0.60	−0.38	RCW	−31.28	BM98	2.36	2.22
Ca I								Eu II							
4425.44	1.88	−0.36	SN75	−30.90	Sun	6.47	6.45	4129.72[f]	0.00	0.22	LWD			0.49	0.53
4578.55	2.52	−0.70	SR81	−30.30	S81	6.37	6.36	4205.02[f]	0.00	0.21	LWD			0.51	0.53
5261.70	2.52	−0.58	SR81	−30.86	S81	6.41	6.38								
5349.46	2.71	−0.31	SR81	−31.45	S81	6.41	6.38								

Notes. ABO—Barklem et al. (2000); BG96—Baumueller & Gehren (1996); B00—K. Butler (private communication), B75—Bielski (1975); BM98—Barklem & O'Mara (1998); GLS—Gehren et al. (2004); K07, K12—R. Kurucz's Web site http://kurucz.harvard.edu/atoms.html; LD89—Lawler & Dakin (1989); LNA—Ljung et al. (2006); LWD—Lawler et al. (2001); MZG—Mashonkina et al. (2008); NIST—Ralchenko et al. (2010); RCW—Reader et al. (1980); S81—Smith (1981); S88—Smith (1988); SGM—Shi et al. (2009); SN75—Smith & O'Neill (1975); SR81—Smith & Raggett (1981); Sun—the solar line-profile fits; WLS—Wood et al. (2013); ZGZ—Zhang et al. (2008).
[a] IS, Sansonetti et al. (1995)
[b] HFS, ZGZ.
[c] HFS, Shi et al. (2014).
[d] HFS, Borghs et al. (1983).
[e] HFS, K07.
[f] HFS, LWD.

nonlocal origin below the thresholds of the ground state and/or low excitation levels, resulting in the overionization, i.e., depleted level populations compared with their TE values. Most investigated lines are weakened in NLTE compared with their LTE strengths, resulting in positive NLTE abundance corrections. They are overall small in the close-to-solar-metallicity stars and grow toward lower metallicity due to decreasing ultraviolet (UV) opacity, resulting in increasing photoionization rates. For given chemical species different lines reveal similar NLTE effects in a given model atmosphere. An exception are lines of Ca I; see the next paragraph. Pronounced NLTE effects for the resonance in contrast with the subordinate lines were found for Al I. For example, $\Delta_{\rm NLTE}({\rm Al\,I}\ \lambda3961) = 0.77$ dex, while $\Delta_{\rm NLTE} \leqslant 0.13$ dex for the subordinate lines in the model $5890/4.02/-0.78$. This can be easily understood. The excited levels of Al I, however, are subject to overionization, but are closely coupled to the ground state of the majority species Al II via the charge-transfer reactions Al I(nl) + H I(1s) ↔ Al II(3s^2) + H$^-$ (Belyaev 2013), resulting in small $\Delta_{\rm NLTE}$ for Al I $\lambda\lambda6696, 6698, 7835, 7836, 8772, 8773$. The ground state of Al I is separated by 3.14 eV in energy from the excited levels, and its population is mainly decided by overionization. It is worth noting that the NLTE correction for Al I $\lambda3961$ is strongly surface gravity dependent. For example, $\Delta_{\rm NLTE} = 0.20$ and 0.36 dex for the two least luminous and $[{\rm Fe/H}] \simeq -2$ stars BD +66°0268 $(5300/4.72/-2.06)$ and BD +29°2091 $(5860/4.67/-1.91)$, while $\Delta_{\rm NLTE}$ ranges between 0.48 and 0.61 dex for the remaining $[{\rm Fe/H}] < -0.5$ stars.

As discussed in detail by Mashonkina et al. (2007a) and Mashonkina (2013), lines of the photoionization-dominated minority species Ca I and Mg I can have negative $\Delta_{\rm NLTE}$ in the close-to-solar-metallicity models and positive correction in the low-metallicity models (Ca I $\lambda\lambda5349, 5588$ and Mg I $\lambda5528$ in Figure 2). Here, we review briefly. The obtained NLTE abundance appears to be lower than the corresponding LTE one, if the line core forms in the layers, where the departure coefficient of the upper level drops rapidly due to photon escape from (usually) the line itself, resulting in dropping the line source function below the Planck function and enhanced absorption in the line core. In contrast, in the line wings, absorption is weaker compared with the LTE case due to overall overionization in deep atmospheric layers. The net effect is determined by a competition of the NLTE effects in the line core and the line wings. A similar NLTE mechanism leads to slightly negative $\Delta_{\rm NLTE}$ for some lines of Al I, Si I, and Cu I.

2. The collision-dominated minority species Li I, Na I, and K I. In the stellar parameter range, with which we are concerned, these species are subject to the overrecombination resulting in strengthened lines of Li I, Na I, and K I and negative NLTE abundance corrections. The origin of the overpopulation of the ground and first excited state is the photon suction process described in detail by Bruls et al. (1992). The departures from LTE are larger for K I than Na I and larger for Na I than Li I because of smaller photoionization cross sections for K I than Na I and smaller ones for Na I than Li I. The magnitude of $\Delta_{\rm NLTE}$ is small for the Na I resonance lines in the $[{\rm Fe/H}] > -1.5$ models because the lines are strong and their total absorption is mostly contributed from the line wings formed in deep atmospheric layers, where the departures from LTE are small. It is worth noting that the LTE abundances from Na I $\lambda\lambda5889, 5895$ in the $[{\rm Fe/H}] \leqslant -1.5$ stars were derived using the measured equivalent widths because the line profiles

Figure 2. NLTE abundance corrections for the selected lines in the investigated stars. The Sun is shown by the symbol inside the larger-size open circle.

cannot be fitted under the LTE assumption. Similarly, the LTE potassium abundances of all the stars were also derived using the measured equivalent widths.

3. *The majority species C I, O I, Si II, Ti II, and Fe II, with negative NLTE abundance corrections for the investigated lines.* For each of these species its total number density and population of the ground state keep their TE values throughout the atmosphere. Populations of the excited levels are decided by a competition of the UV radiative pumping transitions, which produce an enhanced excitation in the line-formation layers, and photon losses in the lines, when the line optical depth drops below unity, resulting in an underpopulation of the upper levels of the corresponding transitions. For C I, O I, Si II, Ti II, and Fe II the lower levels of the investigated transitions are overpopulated in line-formation layers, resulting in strengthened lines and negative NLTE abundance corrections. For different lines of Ti II and Fe II Δ_{NLTE} is overall small. In line with the previous NLTE studies of C I (Alexeeva & Mashonkina 2015, and references therein) and O I (Sitnova et al. 2013, and references therein), pronounced NLTE effects were computed for the IR lines in the [Fe/H] > −1.5 models, with Δ_{NLTE} up to −0.5 dex. The NLTE corrections reduce in absolute value toward lower metallicity due to shifting line-formation depth to deep atmospheric layers. For the visible lines of C I and O I Δ_{NLTE} values are overall small because the lines are weak and form in deep atmospheric layers.

4. *The majority species Sc II, Zr II, and Eu II, with positive NLTE abundance corrections for the investigated lines.* Here, for each line, NLTE leads to its weakening relative to the LTE strength, owing to the larger overpopulation of the upper than the lower level relative to the corresponding TE populations, which results in the increase in the line-source function above the Planck function in the line-formation layers.

5. *The majority species Sr II and Ba II, with the sign of the NLTE correction depending on the line and stellar parameters.* As found theoretically by Mashonkina et al. (1999), NLTE may lead either to strengthening or to weakening the Ba II lines depending on stellar parameters and element abundance. In our stellar sample, Δ_{NLTE} is negative for Ba II $\lambda\lambda$5853 and 6496 in the [Fe/H] > −1 and [Fe/H] > −1.8 stars, and it becomes positive at lower metallicity. For Sr II, NLTE leads to a strengthening of the resonance lines and, in contrast, to a weakening of the subordinate line at 4161 Å. This can be understood as follows. In each model, the ground state keeps the TE population throughout the atmosphere and the upper level, 5p, of the resonance transition is underpopulated in the uppermost atmospheric layers due to photon losses in the resonance lines themselves, resulting in an enhanced absorption of the $\lambda\lambda$4077 and 4215 lines. The Sr II λ4161 line arises from the 5p–6s transition, where the upper level is overpopulated to a greater extent with regard to its LTE population than that of the lower level in the line formation layers.

4. DETERMINATION OF STELLAR ABUNDANCES

To minimize the effect of the uncertainty in *gf*-values on the final results, we applied a line-by-line differential NLTE and LTE approach, in the sense that stellar line abundances were compared with individual abundances of their solar counterparts. Throughout this study, the element abundance is

determined from line-profile fitting. The synthetic line profiles were computed with either the code SIU (Reetz 1991) or the codes SYNTHV-NLTE (Ryabchikova et al. 2016) + BIN-MAG3.[15] The metal line list has been extracted from the Vienna Atomic Line Database[16] (VALD3; Ryabchikova et al. 2015). Our test calculations of the C I and Zr II lines in a broad wavelength range from 4209 to 9111 Å in the solar model atmosphere prove that using SIU and SYNTHV-NLTE + BINMAG3 does not produce systematic shifts in derived abundances, namely, the abundance difference nowhere exceeds 0.03 dex.

In order to compare the theoretical profiles with observations, they were convolved with a profile that combines instrumental broadening with a Gaussian profile, rotational broadening, and broadening by macroturbulence with a radial-tangential profile. Rotational broadening and broadening by macroturbulence were treated separately for the six stars with $v \sin i \geqslant 6\,\mathrm{km\,s^{-1}}$, namely, HD 58855 ($v \sin i = 10\,\mathrm{km\,s^{-1}}$), HD 89744 ($9\,\mathrm{km\,s^{-1}}$), HD 92855 ($10\,\mathrm{km\,s^{-1}}$), HD 99984 ($6\,\mathrm{km\,s^{-1}}$), HD 100563 ($10\,\mathrm{km\,s^{-1}}$), and HD 106516 ($7\,\mathrm{km\,s^{-1}}$). We treated the overall effects of rotation and macroturbulence for the remaining stars as radial-tangential macroturbulence. The $v \sin i$ values and most probable macroturbulence velocities V_{mac} were determined in this study from the analysis of an extended list of lines of various chemical species. For a given star, V_{mac} was allowed to vary by ±0.4 km s^{-1} (1σ). We selected a mildly MP star HD 134169 (5890/4.02/−0.78) to illustrate in Figure 3 a quality of the line fits in a broad spectral range from 4077 to 9078 Å.

We determined abundances of 17 elements from Li to Eu and for silicon from two ionization stages. Table 3 (online material) presents the mean LTE and NLTE abundances, their error bars (σ), and the number of lines used to determine the mean abundances. For most species their abundances are based on analysis of 2–20 lines. An exception is Li I, K I, and Eu II, with a single line measured.

For every species with more than one line measured the differences in differential NLTE abundance between different lines were found to be consistent within 0.05 dex, on average, for the entire stellar sample. Figure 4 displays the abundance differences for the selected pairs of lines. We comment below on individual chemical species.

4.1. Notes on Individual Chemical Species

Lithium. The lithium abundances are derived from the Li I λ6708 resonance line for 42 stars. The remaining nine stars do not have obvious features that are reliable enough for the lithium abundance determinations at 6708 Å. The Li I asymmetric profile shape (see Figure 3 for HD 134169) is mainly caused by the two doublet structure components, Li I λ6707.76 and Li I λ6707.91. They were treated, using atomic data from Shi et al. (2007) with all the HFS components included. Taking all the blended lines in the asymmetric core region into account produces no more than 0.005 dex change in the derived Li abundance, as shown by our test calculations for all the stars with [Fe/H] > −0.2 in our sample. The influence due to the presence of ^{6}Li in all the halo stars is also evaluated. Assuming

---

[15] http://www.astro.uu.se/~oleg/download.html
[16] http://vald.astro.univie.ac.at/~vald3/php/vald.php
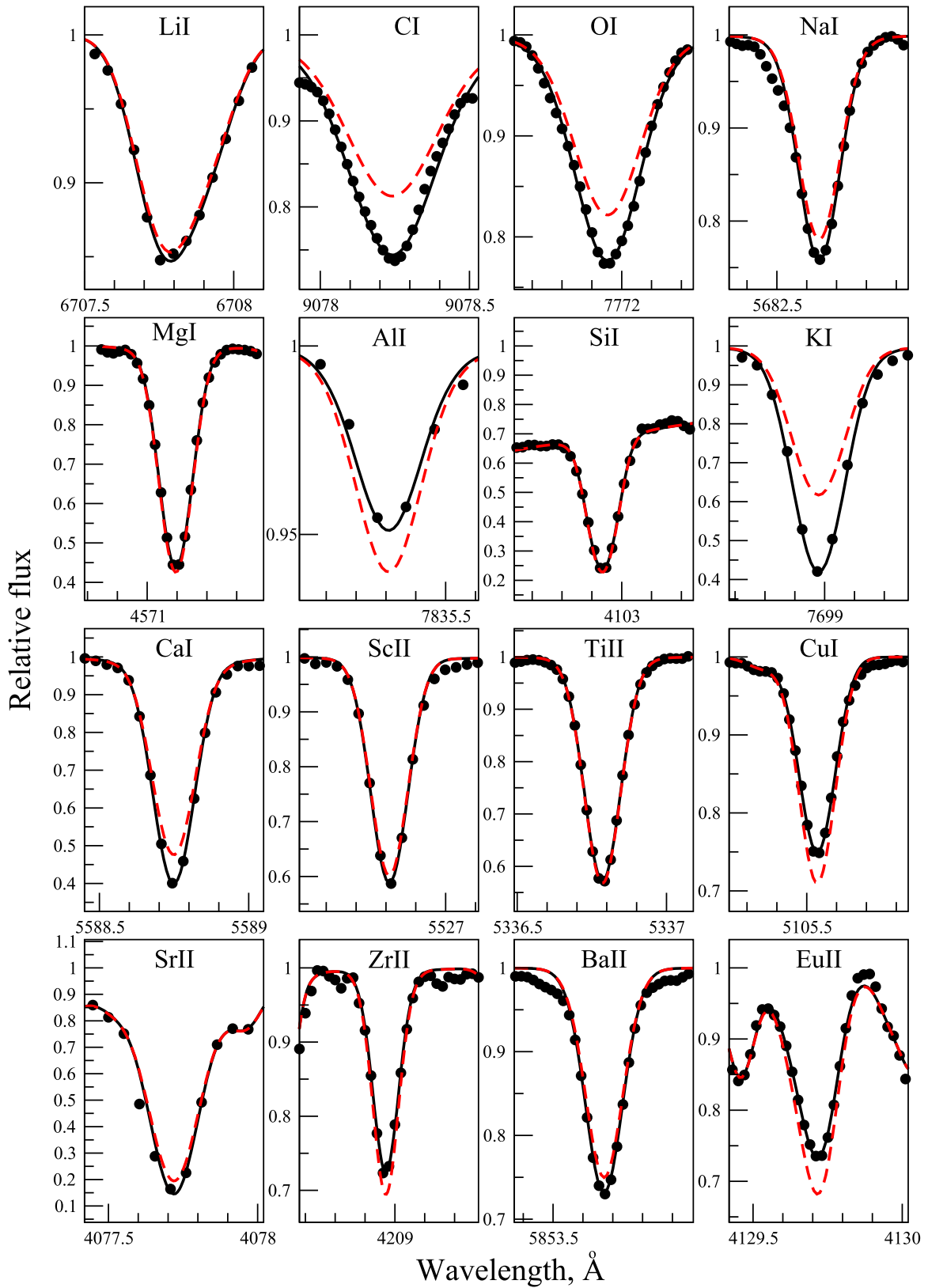
Figure 3. Best NLTE fits (solid curves) of the observed spectrum of HD 134169 (filled circles). For comparison, the LTE profiles computed with the corresponding NLTE abundances are shown by dashed curves.

a meteoric isotopic ratio of 12.3 (^{7}Li/^{6}Li) gives 0.034 dex smaller abundance for Li on average.

Carbon. We used three carbon abundance indicators, namely, the atomic C I and the molecular CH and C$_2$ lines.

Suitable lines of C I are located in the visible and near-IR spectral range (Table 2). They all have a similar excitation energy of the lower level, E_{exc}, but different oscillator strengths, with smaller values for the visible than the near-IR

Table 3
Summary of the Obtained Stellar Abundances

Z	Species	N	LTE		NLTE		Z	Species	N	LTE		NLTE	
			[X/H]	[X/Fe]	[X/H]	[X/Fe]				[X/H]	[X/Fe]	[X/H]	[X/Fe]
		HD 19373	6045/4.24/ 0.10, $\xi_t = 1.2$		Thin disk				HD 22484	6000/4.07/0.01, $\xi_t = 1.1$		Thin disk	
3	Li I	1	2.50		2.47		3	Li I	1	2.37		2.33	
6	C I	5	-0.00 ± 0.04	-0.10	-0.05 ± 0.05	-0.15	6	C I	5	-0.07 ± 0.04	-0.08	-0.09 ± 0.04	-0.10
⋯	CH	13	0.10 ± 0.06	0.00	⋯	⋯	⋯	CH	13	0.07 ± 0.03	0.06	⋯	⋯
8	O I	4	0.01 ± 0.01	-0.09	-0.06 ± 0.04	-0.16	8	O I	4	0.01 ± 0.06	0.00	-0.07 ± 0.05	-0.08
11	Na I	4	0.27 ± 0.06	0.17	0.21 ± 0.04	0.11	11	Na I	4	0.03 ± 0.09	0.02	-0.01 ± 0.07	-0.02
12	Mg I	5	0.12 ± 0.02	0.02	0.11 ± 0.02	0.01	12	Mg I	5	0.00 ± 0.04	-0.01	0.00 ± 0.03	-0.01
13	Al I	2	0.08 ± 0.02	-0.02	0.10 ± 0.01	0.00	13	Al I	2	-0.13 ± 0.04	-0.14	-0.11 ± 0.03	-0.12
14	Si I	9	0.11 ± 0.03	0.01	0.11 ± 0.03	0.01	14	Si I	9	-0.05 ± 0.05	-0.06	-0.06 ± 0.05	-0.07
14	Si II	2	0.03 ± 0.04	-0.07	0.02 ± 0.04	-0.08	14	Si II	2	-0.02 ± 0.04	-0.03	-0.06 ± 0.05	-0.07
19	K I	1	0.22	0.12	0.05	-0.05	19	K I	1	0.19	0.18	-0.03	-0.04
20	Ca I	18	0.08 ± 0.05	-0.02	0.04 ± 0.05	-0.06	20	Ca I	17	-0.05 ± 0.04	-0.06	-0.09 ± 0.04	-0.10
21	Sc II	9	0.12 ± 0.03	0.02	0.11 ± 0.03	0.01	21	Sc II	9	-0.01 ± 0.03	-0.02	-0.02 ± 0.02	-0.03
22	Ti II	10	0.07 ± 0.03	-0.03	0.07 ± 0.03	-0.03	22	Ti II	8	-0.03 ± 0.04	-0.04	-0.03 ± 0.04	-0.04
26	Fe I	26	0.16 ± 0.07	0.06	0.17 ± 0.07	0.07	26	Fe I	27	-0.01 ± 0.06	-0.02	0.01 ± 0.06	0.00
26	Fe II	15	0.10 ± 0.05	0.00	0.10 ± 0.05	0.00	26	Fe II	16	0.01 ± 0.04	0.00	0.01 ± 0.04	0.00
29	Cu I	3	0.18 ± 0.02	0.08	0.16 ± 0.02	0.06	29	Cu I	3	-0.07 ± 0.02	-0.08	-0.07 ± 0.02	-0.08
38	Sr II	2	0.04 ± 0.08	-0.06	0.02 ± 0.05	-0.08	38	Sr II	2	-0.05 ± 0.08	-0.06	-0.07 ± 0.04	-0.08
40	Zr II	2	-0.06 ± 0.03	-0.16	-0.05 ± 0.03	-0.15	40	Zr II	2	0.00 ± 0.06	-0.01	0.01 ± 0.07	0.00
56	Ba II	3	0.04 ± 0.02	-0.06	0.01 ± 0.04	-0.09	56	Ba II	3	0.19 ± 0.03	0.18	0.13 ± 0.03	0.12
63	Eu II	1	-0.10	-0.20	-0.09	-0.19	63	Eu II	1	0.01	0.00	0.02	0.01

(This table is available in its entirety in machine-readable form.)

lines. The C I visible lines were used in the close-to-solar metallicity down to [Fe/H] = −1.5 stars. The IR lines are strong enough to be measured in the entire metallicity range; however, they were not used for HD 64090, BD +66°0268, HD 24289, HD 74000, HD 108177, BD +29°2091, and G090-003 because of strong fringes affecting the near-IR spectra. Consistent within 0.05 dex, NLTE abundances from the visible and near-IR lines were found for most stars, where both groups of lines were measured; see, for example, the abundance differences between C I λλ5052 and 9111 in Figure 4.

For the molecular CH and C₂ lines we use their list together with the atomic parameters from Alexeeva & Mashonkina (2015). The C₂ lines are rather weak and cannot be measured in the [Fe/H] < −0.84 stars, while the CH bands were detected in the entire metallicity range. Exceptions are the hottest stars HD 100563, BD −13°3442, BD −04°3208, and BD +24° 1676. We obtained small abundance shifts of 0.02 ± 0.10 dex, on average, between the molecular CH and atomic C I (NLTE) lines (Figure 5). Applying the 3D corrections from Gallagher et al. (2016) to the CH G band decreases the scatter of abundance differences only a little, resulting in CH(3D) − C I = 0.01 ± 0.085. The mean abundance difference between C I and C₂ amounts to −0.04 ± 0.05.

Despite the fact that atomic and molecular lines give consistent results, we prefer to employ the C I-based abundances for final carbon abundances. The CH-based abundances were employed for the stars with [Fe/H] < −1, with no C I line measured.

Oxygen. Determination of the element abundances from the O I IR lines takes advantage of using the spectra with removed fringes, as described in Section 2. Employing only the visible O I λ6158 line would restrict our O abundance analysis to the [Fe/H] = −0.5 stars, where this line can be measured. All the

O I lines give abundances consistent within the error bars, as shown in Figure 4 for O I λλ7771 and 6158.

Sodium abundances were determined using six Na I lines, including the strong Na I D lines, because for some very metal-poor stars only the Na I D lines could be used for abundance determination. However, for stars with [Fe/H] > −0.5, the Na I D lines (λλ5889 and 5895) were not used in calculating the final average abundances.

Magnesium abundances were determined using five neutral Mg lines, as shown in Table 1. The strong Mg I b lines were not employed for abundance determination.

Aluminum. Determining Al abundances is very challenging for our sample stars. We used seven lines of Al I. However, for most stars their Al abundance is based on the resonance line, Al I λ3961, or the subordinate lines in the red and IR spectral region. The resonance line is strong enough to be detected in all the sample stars. However, this line falls in the wing of a strong Ca II λ3968 line, which makes the normalization very difficult for the close-to-solar-metallicity stars. The other six lines in the near-IR in the Shane/Hamilton spectra suffer from the fringing effect. For HD 59374, HD 59984, and HD 134169 we used their high-quality FOCES spectra and could measure five to seven lines of Al I. For each star the LTE analysis obtained a 0.25–0.45 dex lower element abundance from the resonance line compared with that from the subordinate lines. Thanks to implementing quantum mechanical data on Al I+H I collisions by Belyaev (2013) in the SE calculations (Mashonkina et al. 2016), an abundance discrepancy between different lines was largely removed in NLTE.

Silicon. We applied 11 Si I and two Si II lines to derive the Si abundances. Two strong ultraviolet Si I lines, λλ3905 and 4102, were not used for the stars with [Fe/H] > −0.5 because of the saturation, while for the six most MP stars, only these two lines can be used for the abundance determination.
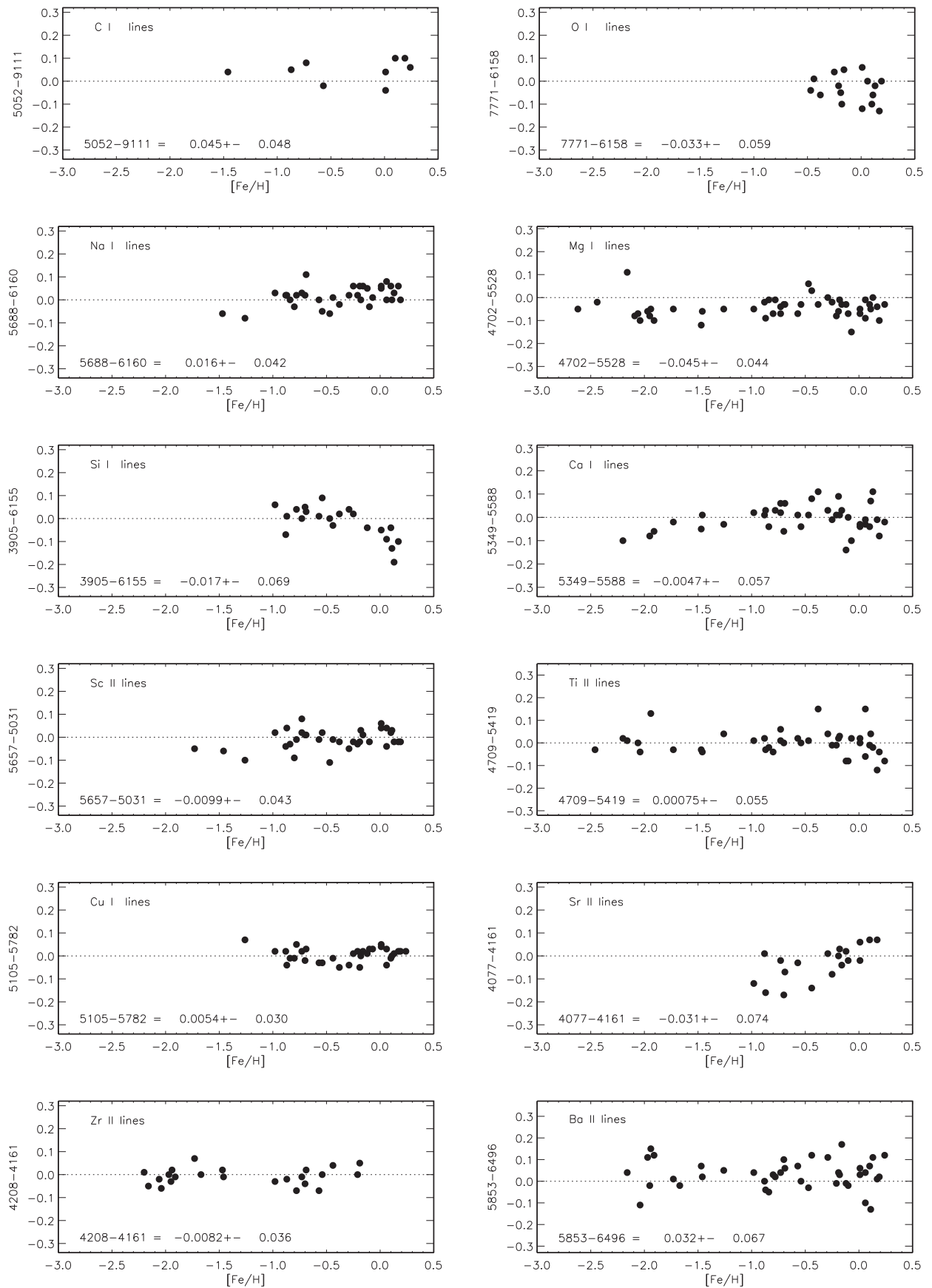
Figure 4. Differences in differential NLTE abundance between individual lines. The mean difference, together with the standard deviation, is quoted in each panel.

It is worth noting that lines of Si I and Si II lead to consistent NLTE abundances, with the mean difference (Si I–Si II) = 0.00 ± 0.05 dex for our 32 program stars. The final results are the average abundances of Si I and Si II.

Potassium. Abundances of K were obtained by using the K I $\lambda7699$ line, whereas the $\lambda7664$ line is heavily blended with the telluric O_2 lines for most sample stars. The potassium lines are also affected by very strong fringing effects. Hence, we could not determine potassium abundances for most very metal-poor stars with [Fe/H] < −2.0.

Calcium. Among investigated elements in this paper, calcium covers many visible lines, and 21 Ca I lines were employed in our abundance determination. The Ca I resonance line at 4226 Å is very strong in all our program stars, and it was not used in the abundance analysis. For stars with [Fe/H] > −0.5 dex we also did not include Ca I $\lambda\lambda6162$ and 6439, when calculating the average Ca abundance, because of their saturation.

Scandium. Because the Sc I lines in metal-poor stars are extremely week, the nine lines of Sc II are employed in the abundance determinations, although the number of lines is decreased to 1–3 for very metal-poor stars. Again, the NLTE corrections for all Sc II lines are small.

Titanium. For final Ti abundances we prefer to employ lines of Ti II because of small NLTE effects. Indeed, $\Delta_{\rm NLTE} \leqslant 0.02$ dex, in absolute value, everywhere for the Ti II lines in our calculations.

Copper. We applied three Cu I lines for determinations of copper abundances, namely, $\lambda\lambda5105$, 5218, and 5782, which are the same as in our very recent study (Yan et al. 2016). Among them, $\lambda5105$ is the strongest and least blended line (the only weak Fe II line at the very blue wing) and thus is a good indicator of the copper abundance. The $\lambda5218$ line is weak, and its blue wing is blended by an Fe I line, which usually has a comparable equivalent width with the Cu I line. We thus took the two lines together into consideration during the line-profile fitting. The $\lambda5782$ line is also blended by several weak lines (i.e., Cr I, Cr II, Fe I, Fe II). Taking all the lines into account gives a consistent copper abundance with the other two lines. The Cu abundance difference between including and ignoring the blended lines near 5782 Å is ∼0.02 dex, on average. The Cu I lines are weakened toward lower metallicity, and no copper abundance can be derived from these three lines for stars with [Fe/H] < −1.5.

Strontium. Three lines of Sr II were employed in the abundance determinations. The subordinate line at 4161 Å was measured in the [Fe/H] $\geqslant$ −0.98 stars, and it gives an Sr abundance in line with that from Sr II $\lambda4077$, with a mean difference of 0.03 ± 0.07 dex for 19 common stars (Figure 4). The Sr II $\lambda4215.5$ line is heavily blended by Fe I $\lambda4215.426$ and by a few CN molecular lines in the far blue and red line wings, and it was not used for the [Fe/H] > −1 stars. In the more MP stars, the two resonance lines give consitent abundances, with Sr II $\lambda4077$–Sr II $\lambda4215$ = −0.01 ± 0.08 for 17 common stars.

Zirconium. Only three lines of Zr II are suitable for stellar abundance determinations. The Zr II $\lambda4208.98$ line is strong enough to be measured in the entire range of metallicity. An exception is our most MP star BD −13°3442 ([Fe/H] = −2.62), where no Zr II line was detected. To account for the blending Cr I $\lambda4208.95$ line ($E_{\rm exc}$= 3.85 eV, log *gf* = −0.528 according to VALD) correctly, we controlled the chromium

LTE abundance using a nearby line of Cr I $\lambda4209.365$, with $E_{\rm exc}$= 3.85 eV and log *gf* = −0.263 (VALD). In contrast, Zr II $\lambda5112$ is unblended, but it is weak and can only be measured in the [Fe/H] > −0.88 stars. Another line, Zr II $\lambda4161.21$, is located in the red wing of Fe I $\lambda4161.08$. The blending effect reduces toward lower metallicity, and Zr II $\lambda4161$ provides a reliable abundance at [Fe/H] < −0.19. We obtained consistent abundances from all the lines, with a mean abundance difference of −0.0 1 ± 0.04 dex between Zr II $\lambda\lambda4208$ and 4161 and of 0.00 ± 0.06 dex between Zr II $\lambda\lambda4208$ and 5112.

Barium. For the majority of stars their barium abundance was determined from the Ba II subordinate lines, which are almost free of HFS effects. According to our estimate for Ba II $\lambda6497$, neglecting HFS makes a difference in the solar abundance of no more than 0.01 dex. We avoided employing the Ba II $\lambda\lambda4554$ and 4934 resonance lines for the [Fe/H] > −2 stars, where they are saturated and the derived element abundance depends on the Ba isotope mixture adopted in the calculations because the lines are strongly HFS affected. In the three most MP stars, HD 140283, BD +24°1676, and BD −13°3442, the subordinate lines of Ba II cannot be extracted from noise, and the barium abundance given in Table 3 was determined from the resonance lines. It is worth noting that Ba II $\lambda\lambda4554$ and 4934 are rather weak in each of these stars, and a change in the Ba abundance derived from these lines does not exceed a few hundredths when moving from the solar mixture ^{134}Ba:^{135}Ba:^{136}Ba:^{137}Ba:^{138}Ba = 2.4:6.6:7.9:11.2:71.7 (Lodders et al. 2009, pp. 44–54) to the *r*-process one ^{135}Ba:^{137}Ba:^{138}Ba = 24:22:54 (Travaglio et al. 1999). For example, Ba II $\lambda4554$ in HD 140283 has an equivalent width (EW) of 20 mÅ, and the abundance shift between using the solar and the *r*-process Ba isotope mixture amounts to 0.02 dex.

Europium. Three lines of Eu II were employed in the abundance determinations. The subordinate line at 6645 Å was measured in the [Fe/H] $\geqslant$ −0.78 stars, and it appears to give systematically higher abundance compared with that from Eu II $\lambda4129$, with a mean difference of 0.14 ± 0.13 dex for 17 common stars. This line was nowhere used to obtain the final Eu abundance. The resonance line of Eu II at 4204.878–4205.117 Å is blended by numerous metal lines, which cannot be taken into account correctly even using the synthetic spectrum approach. As a result, the abundance difference between Eu II $\lambda\lambda4129$ and 4205 was obtained to be −0.06 ± 0.06 dex for 37 common stars. We avoided using Eu II $\lambda4205$ in a determination of the final Eu abundance. Exceptions are the six stars with [Fe/H] between −1.73 and −2.20, where Eu II $\lambda4129$ could not be measured due to either strong blending by the SiH $\lambda\lambda4129.609$, 4129.666, 4129.774 lines in the cool dwarfs HD 64090 and BD +66°0268 or a bad quality of the observed spectra. No line of Eu II can be extracted from noise in our more MP stars.

4.2. Uncertainties in Derived Abundances

We choose a mildly metal-deficient star HD 134169 ([Fe/H] = −0.78) to perform a detailed error analysis and to estimate the uncertainties in the abundance measurements for all the investigated species. Stochastic errors ($\sigma_{\rm obs}$) caused by random uncertainties in the continuum placement, line-profile fitting, and *gf*-values are represented by a dispersion in the measurements of multiple lines around the mean, as given in Table 3 when $N \geqslant 2$ lines of an element are observed. Systematic

Table 4
Error Budget for Elements in HD 134169

Atom	σ_{obs}	λ (Å)	ΔT −80 K	Δlo-g g 0.07	$\Delta\xi$ −0.1 km s^{-1}	Δ (T, g, ξ)
(1)	(2)	(3)	(4)	(5)	(6)	(7)
Li I	⋯	6707	−0.08	−0.01	0.01	0.08
C I	0.01	5380	0.06	0.04	0.00	0.07
O I	0.01	7771	0.06	0.02	0.00	0.06
Na I	0.04	5688	−0.02	0.02	0.00	0.03
Mg I	0.04	5528	−0.07	−0.04	0.01	0.08
Al I	0.10	8772	−0.05	−0.02	0.00	0.05
Si I	0.05	6145	0.00	0.03	0.00	0.03
K I	⋯	7698	0.02	0.02	0.03	0.04
Ca I	0.05	5588	−0.02	0.01	0.03	0.04
Sc II	0.03	5526	−0.11	−0.07	0.02	0.13
Ti II	0.03	5336	−0.01	0.04	0.04	0.06
Cu I	0.03	5218	0.01	0.07	0.00	0.07
Sr II	0.06	4077	−0.04	0.01	0.01	0.04
Zr II	0.05	4208	−0.01	0.04	0.01	0.04
Ba II	0.01	6496	0.01	0.04	0.06	0.07
Eu II	⋯	4129	−0.02	0.04	0.00	0.04

uncertainties include those that exist in the adopted stellar parameters. Table 4 summarizes the various sources of uncertainties. For each species we choose a representative line indicated in column (3) to calculate an abundance shift due to a change of −70 K in T_{eff}, +0.07 dex in log g, and −0.1 km s^{-1} in ξ_t. The quantity $\Delta(T, g, \xi)$ listed in column (7) is the total impact of varying each of the three parameters, computed as the quadratic sum of columns (4)–(6).

4.3. Notes on Individual Stars

Planet-host stars. In our sample, five stars have been reported to harbor one or more planets according the catalog listing of the Extrasolar Planets Encyclopaedia.[17] Three of them, HD 30562, HD 82943, and HD 89744, are metal-rich stars with [Fe/H] ≃ 0.1–0.2 dex, while HD 115617 and HD 142091 have solar or slightly subsolar metallicities. We did not detect any special characteristics in element abundance ratios for these planet-host stars.

Stars with thin-disk kinematics but thick-disk chemistry. Our two most MP stars with thin-disk kinematics, HD 105755 ([Fe/H] = −0.73) and HD 134169 ([Fe/H] = −0.78), reveal α- and r-process enhancements typical of the thick-disk stars, with [Mg/Fe] = 0.29 and 0.34 and [Eu/Ba] = 0.50 and 0.51.

Halo star HD 74000 ([Fe/H] = −1.97) reveals typical abundances of the α-process elements, but overabundance of sodium and underabundance of europium compared with the stars of similar metallicity (Figures 8, 10, 11, 13, and 14). We selected HD 24289 ([Fe/H] = −1.94) to show a difference in element abundance pattern between HD 74000 and the [Fe/H] ≃ −2 stars (Figure 6). Its peculiar [Na/Fe], [Na/Mg], [Eu/Fe], and [Eu/Ba] ratios were reported earlier by Gehren et al. (2004) and Mashonkina et al. (2003). This star is also known for its extreme nitrogen overabundance, with [N/Fe] = 0.9 (Carbon et al. 1987), and probably not representative of a standard evolutionary scenario for our Galaxy.

Halo star G090-003 ([Fe/H] = −2.04). We draw attention to high abundances of Na and Al in this star. The Na I resonance

─────────
[17] http://exoplanet.eu/catalog/
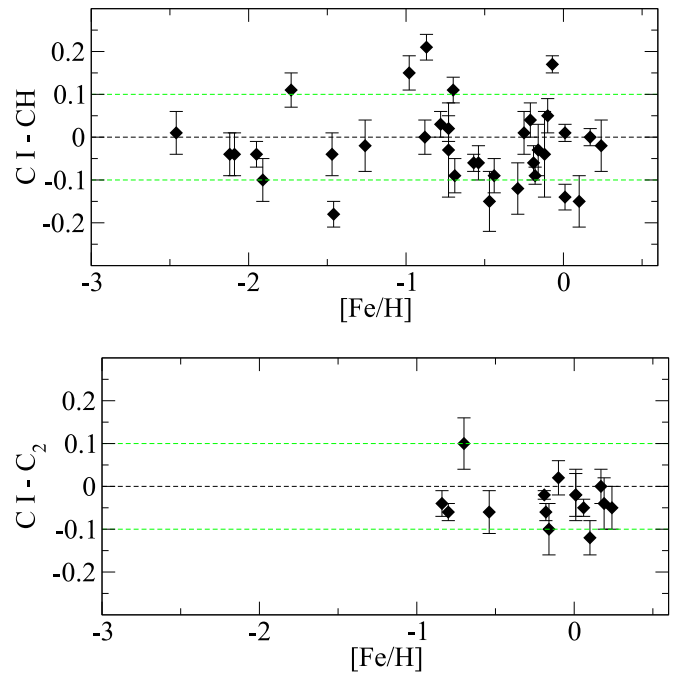
Figure 5. Differences in abundance derived from lines of C I in NLTE and molecular lines of CH (top panel) and C_2 (bottom panel) in the investigated stellar sample.
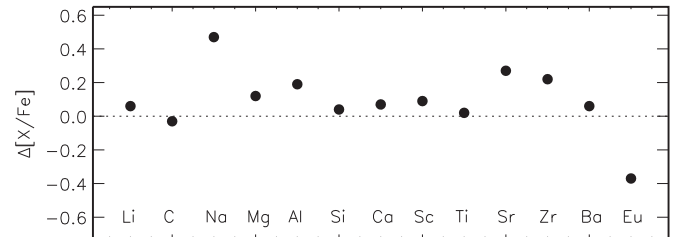
Figure 6. Differences in element abundance ratios, [X/Fe], between HD 74000 and HD 24289. All the results are from the NLTE calculations.

lines in its observed spectrum are both affected by emissions of, probably, telluric origin. Since the quality of the spectrum of G090-003 is very good, we could measure the Na abundance from Na I λ5688. This gives a nearly 0.2 dex lower abundance compared with that from the resonance lines; however, it is still large. Although the Na and Al abundances in G090-003 are higher than those in stars of similar metallicity, their ratio is close to the solar one, like in other stars (Figure 11).

5. THE GALACTIC CHEMICAL EVOLUTION

5.1. Stellar Abundance Trends

Stellar abundances for different elements, classified from their nucleosynthesis histories, for a large sample of stars with different metallicities play a key role in the study of the chemical evolution of these elements themselves, their origins, and the chemical evolution of the Galaxy. This study is of particular importance because it presents, for the first time, abundances of many elements in a broad metallicity range that were homogeneously derived from the NLTE analysis. Among all the investigated species, lithium holds a specific position, because it is of primordial origin and considered a key diagnostic to test and constrain our description of the early

13
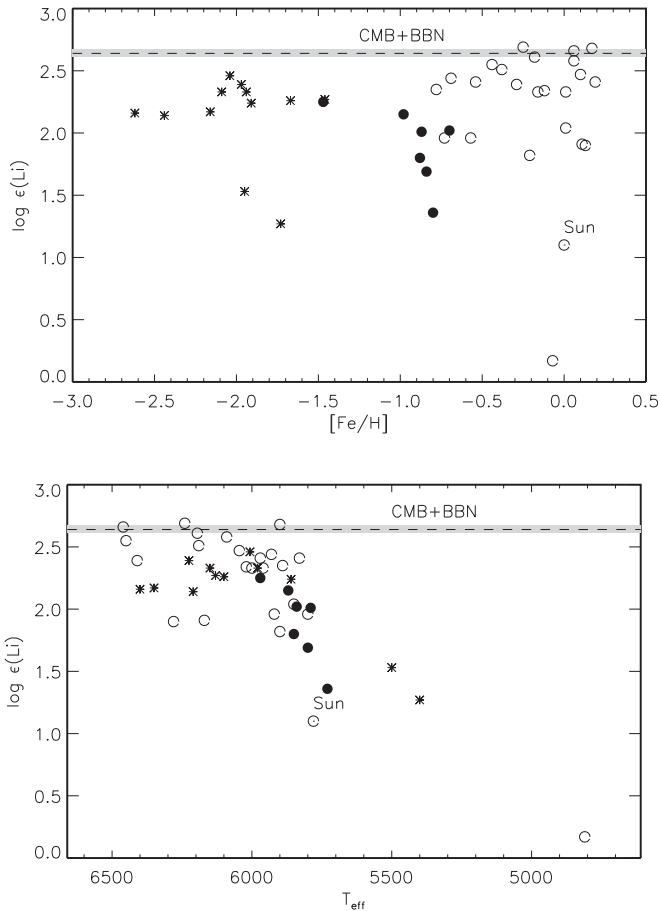
Figure 7. Stellar NLTE abundances of Li as a function of metallicity (top panel) and effective temperature (bottom panel). Different symbols correspond to different stellar populations, namely, the thin disk (open circles), the thick disk (filled circles), and the halo (asterisks). The dashed line and shaded area show the predicted primordial lithium abundance, $\log \varepsilon_{Li}$(CMB+BBN) = 2.64 ± 0.03 (Spergel et al. 2007).

Galaxy, of stellar interiors and evolution, and of spallation physics. Elements beyond carbon are of stellar origin. Their abundances suffer from the so-called even–odd effect, which gives rise to different yields for different elements despite their same nucleosynthesis path. Therefore, in the C–Ti range we group the even-nuclear charge (Z) elements and the odd-Z elements. Elements beyond the iron group are believed to be produced in the neutron-capture nuclear reactions. We discuss separately Sr–Eu and copper, because for the latter its production mechanisms are still debated.

Lithium. We found that Li abundances of the warm ($T_{eff} \geqslant$ 5800 K) halo stars are surrounding the well-defined plateau at $\log \varepsilon_{Li} = 2.2$ (Figure 7). This is in line with the earlier discovery of a remarkably flat and constant Li abundance among Galactic halo dwarf stars spanning a wide range of effective temperatures and metallicities—the so-called Spite plateau (Spite & Spite 1982). Careful reanalysis of the literature data led Charbonnel & Primas (2005) to deduce $\log \varepsilon_{Li} = 2.177 \pm 0.071$ for the [Fe/H] $\leqslant -1.5$ stars with $T_{eff} \geqslant$ 5700 K. With the baryon-to-photon ratio defined accurately by the *Wilkinson Microwave Anisotropy Probe*, standard big bang nucleosynthesis (BBN) predicts a primordial lithium abundance of $\log \varepsilon_{Li} = 2.64 \pm 0.03$ (Spergel et al. 2007) to 2.72 ± 0.06 (Coc et al. 2012). Several physical mechanisms were proposed to reduce the Li abundance at the

surface of halo stars compared with the pristine one (see, e.g., Charbonnel & Primas 2005; Korn et al. 2006; Fu et al. 2015); however, the theoretical models see considerable difficulties in reconciling a non-negligible depletion of lithium with both the flatness and the small dispersion along the Spite plateau. It is worth noting that the NLTE corrections for the only line, Li I λ6707, used in the abundance determinations are mostly negative and small in absolute value (Figure 2). Our two coolest ($T_{eff} \leqslant$ 5500 K) halo stars have a more than 0.7 dex lower Li abundance compared with the Spite plateau. Similar temperature dependence was already noticed by Charbonnel & Primas (2005), and they suggested that "the most massive of the halo stars have had a slightly different Li history than their less massive contemporaries."

The Li abundances of the thick-disk stars are very similar to those of halo stars of similar temperature. This puts strong constraints on the possible Li depletion mechanism(s). In the thin-disk stars $\log \varepsilon_{Li}$ varies between 1.8 and 2.7, and a temperature dependence is not evident. An outlier is the cool giant HD 142091 ($T_{eff} = 4810$ K, $\log g = 3.12$), where $\log \varepsilon_{Li}$ = 0.17, in line with the star's evolutionary status. We confirm the existence of the Li desert at $T_{eff} \simeq 6000$ K and $\log \varepsilon_{Li} \simeq 1.8$, as found by Ramírez et al. (2012).

Even-Z elements. Carbon abundance increases relative to the Fe one, when metallicity decreases from supersolar values down to [Fe/H] $\simeq -0.8$ (Figure 8), and reaches [C/Fe] = 0.21 ± 0.06, on average, in the thick-disk stars. A substantial scatter of [C/Fe] in the halo stars seems to be due to including stars with the C abundance derived from the molecular CH lines. For example, the lowest [C/Fe] values of −0.11 and 0.03 were obtained for HD 103095 and BD +66°0268, respectively. However, this is not supported by analysis of the [C/O] ratios (Figure 9). The stars of similar metallicity show very similar [C/O] ratios, independent of whether the C abundance is based on the CH or C I lines.

Carbon NLTE abundances were calculated by Fabbian et al. (2006, hereafter, F06) for a sample of $-3.2 <$ [Fe/H] < -0.7 dwarfs, using observations of Akerman et al. (2004). The [C/Fe] NLTE ratios were obtained to be close to the solar one, in contrast to our results. We consider two sources of this discrepancy. The first one is a different treatment of inelastic collisions with H I atoms. The final carbon NLTE abundances were obtained by F06 assuming negligible collisions with hydrogen. We did include collisions with H I and used S_H = 0.3. The abundance difference between applying S_H = 0 and 0.3 is non-negligible. Calculations of F06 with S_H = 0 resulted in 0.1–0.15 dex lower abundances compared with those for S_H = 1 (Figure 9 in F06). Our calculations with S_H = 0, 0.3, and 1 show that the abundance difference between applying S_H = 0 and 1 is larger than that between S_H = 0.3 and 1. For example, in HD 59374 (5850/4.38/−0.88) $\Delta \log \varepsilon(S_H = 1 - S_H = 0)$ = 0.08 dex, while it equals 0.03 dex when comparing the S_H = 1 and 0.3 based abundances. The second source of discrepancy concerns, probably, with a different treatment of background opacity. As shown by Alexeeva & Mashonkina (2015), their NLTE abundance corrections agree well with those of F06 in the [Fe/H] $\geqslant -1$ model atmospheres, when applying the common S_H = 1, and they are less negative at lower metallicities, by 0.08 dex in the 6000/4/−2 model and by 0.16 dex at [Fe/H] = −3. Our test calculations show that a variation in background opacity, for example, excluding H_2^+, metal lines, and quasi-H_2 molecular absorption, can lead to
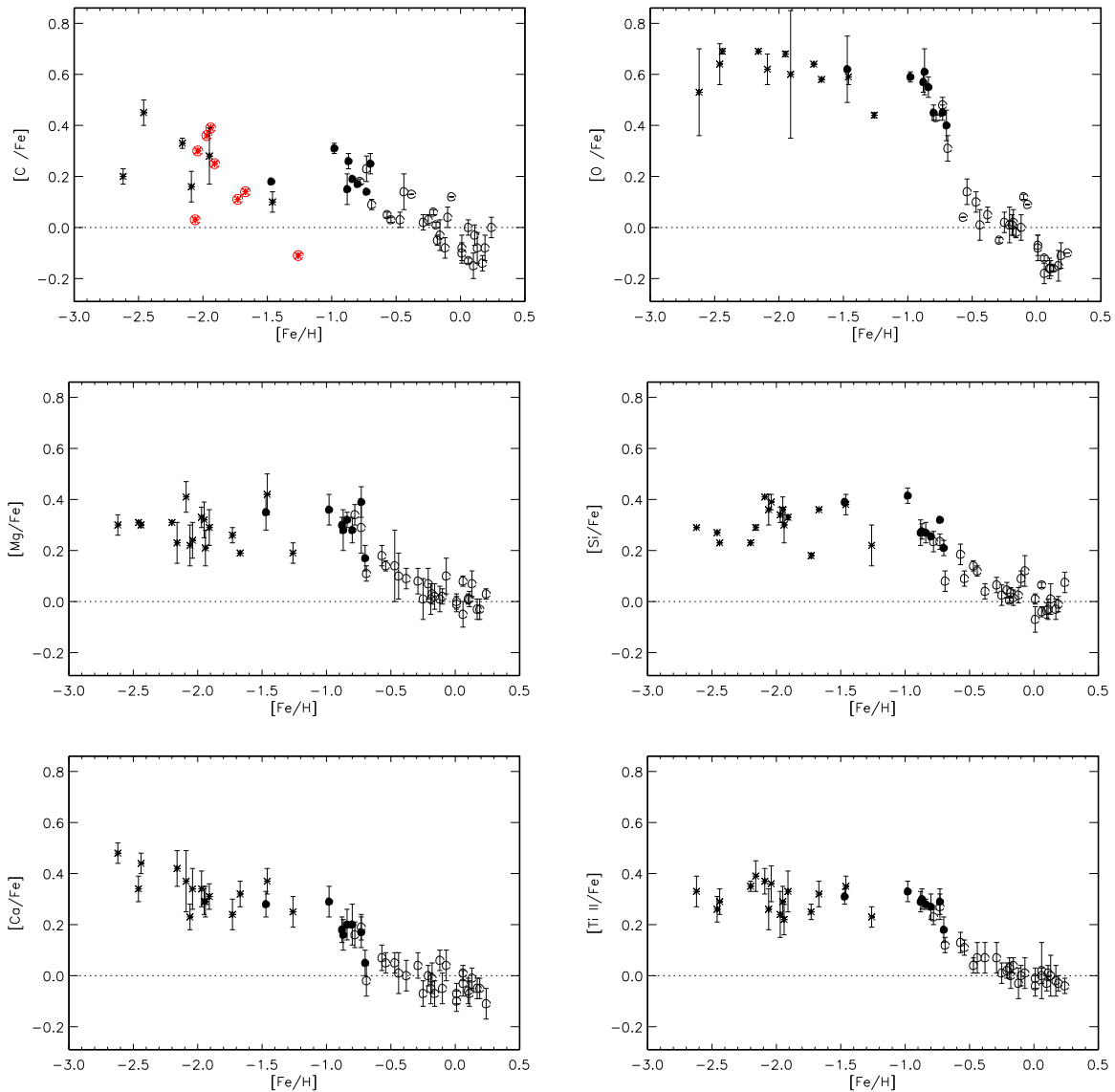
Figure 8. Stellar element-to-iron NLTE abundance ratios: even-Z elements C, O, Mg, Si, Ca, and Ti. The same symbols are used as in Figure 7. Asterisks inside the circles show the halo stars with only the molecular CH lines available.

stronger departures from LTE and to 0.2 dex more negative NLTE corrections for lines of C I in the 5777/3.70/−2.38 model.

Oxygen-to-iron NLTE abundance ratios in stars more metal-poor than $[Fe/H] \simeq -0.9$ form a plateau at $[O/Fe] = 0.61$, with a rather small scatter at a given metallicity (Figure 8). An exception is the halo star HD 103095, which has a 0.16 dex lower O/Fe ratio. For higher metallicity, [O/Fe] shows a downward trend that continues up to supersolar metallicities. It can be seen that the thick-disk and thin-disk stars reveal a common behavior in the overlapping metallicity range, although it is rather narrow. Our results agree well with those of Bensby et al. (2014), who applied the empirical formula to take the NLTE effects into account. However, a scatter of our data for stars of similar metallicity is certainly smaller. Amarsi et al. (2015) inferred a similar value of $[O/Fe] \simeq 0.5$ in the $-2.5 \leqslant [Fe/H] < -1$ range using stellar parameters and observed equivalent widths of the O I lines from the literature and performing detailed 3D NLTE radiative transfer calculations.

From LTE analysis of the $-3.2 \leqslant [Fe/H] \leqslant -0.7$ dwarf and subgiant stars, Akerman et al. (2004) deduced that "C/O drops by a factor of 3–4 as O/H decreases from solar to about 1/10 solar," in line with the earlier findings (see references in Akerman et al. 2004). Their new result was a discovery of the upturn in C/O at $[O/H] = -1$. Having applied the NLTE corrections to the LTE abundances of Akerman et al. (2004), F06 recovered a similar behavior of C/O, with the upturn at $[Fe/H] \simeq -1.2$, where $[C/O] \simeq -0.6$ to -0.7 depending on the S_H value and grows at lower metallicities. Our data are qualitatively similar, namely, C/O is, on average, solar in the thin-disk stars with $[Fe/H] > -0.6$ and decreases steeply at lower metallicities, down to $[C/O] = -0.55$ at $[Fe/H] = -1.26$ (Figure 9). We confirm the upturn in [C/O] at $[Fe/H] \simeq -1.2$. The 11 more metal-poor stars form a linear regression of $[C/O] = -0.78 - 0.19 [Fe/H]$, with $\sigma = 0.06$. The observed C/O trend is important for better understanding nucleosynthesis in the early Galaxy.

Multiple abundance determinations can be found in the literature for Mg, Si, Ca, and Ti. However, homogeneous
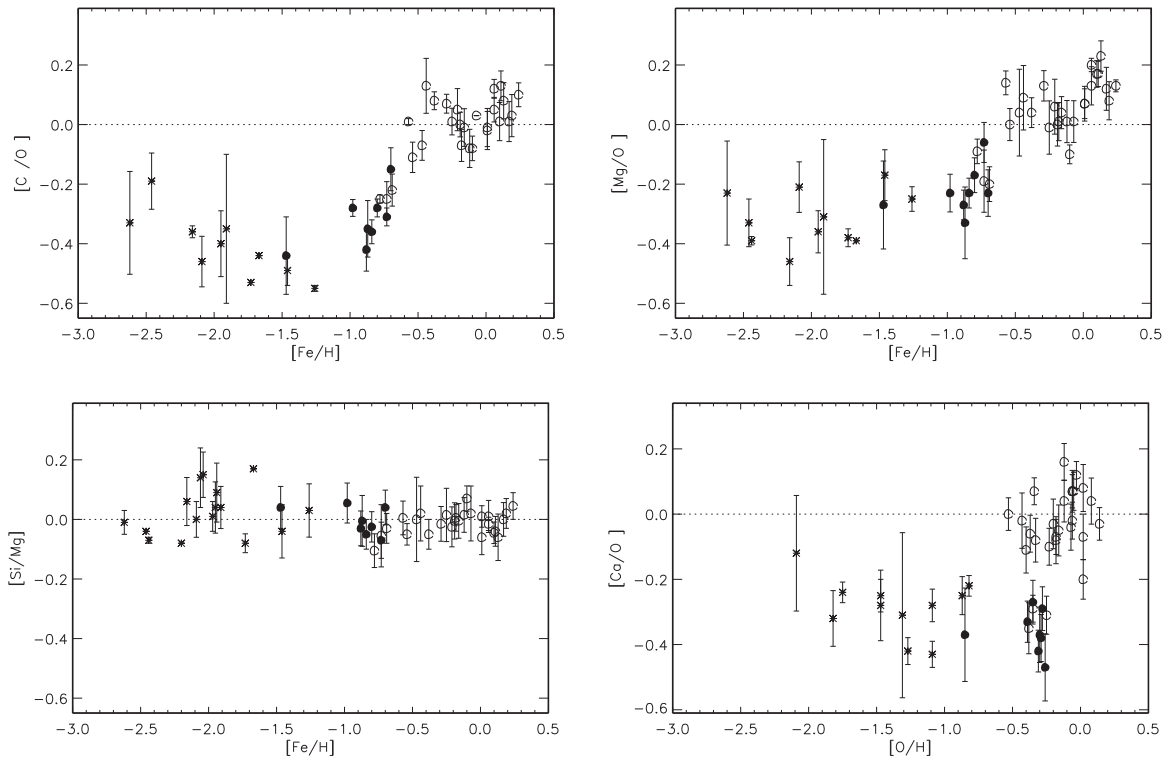
Figure 9. Stellar NLTE abundance ratios between the even-Z elements. The same symbols are used as in Figure 7.

NLTE abundances of all four species and also oxygen in the stellar sample covering a broad metallicity range were obtained in this study for the first time. Magnesium, silicon, calcium, and titanium reveal a common behavior that is typical of the α-process elements. They are enhanced relative to Fe in the halo and thick-disk stars, with nearly constant [X/Fe] ratios at [Fe/H] < −0.8 and similar for different elements (Figure 8). For example, 16 halo stars have, on average, [Mg/Fe] = 0.28 ± 0.07, [Si/Fe] = 0.31 ± 0.07, and [Ti/Fe] = 0.30 ± 0.05. For [Ca/Fe] there is a hint of it increasing toward lower metallicity. The mean amounts to [Ca/Fe] = 0.32 ± 0.08. For each element [X/Fe] decreases at [Fe/H] > −0.8 and reaches the solar value at the solar metallicity. In the overlapping metallicity range the thin- and thick-disk stars have similar [α/Fe] ratios.

We obtained that abundance ratios among Mg, Si, Ca, and Ti are close to the solar value, independent of metallicity (see Si/Mg in Figure 9), while each of these elements is deficient relative to oxygen in the halo and thick-disk stars (Mg/O and Ca/O in Figure 9). Most thin-disk stars have, on average, solar [α/O] ratios. Outliers are the three stars HD 59984, HD 105755, and HD 134169, with a thin-disk kinematics, but a low Fe abundance of [Fe/H] = −0.69, −0.73, and −0.78, respectively. Their [α/Fe] and [α/O] ratios suggest a thick-disk origin. A step-like increase of [α/O] in the thick-disk-to-thin-disk transition is, in particular, clearly seen, when plotting these elemental ratios as a function of [O/H].

Obtained [Mg/Fe] ratios of our halo and thick-disk stars are 0.1 dex lower compared with [Mg/Fe] ≃ 0.4 derived for the nearby [Fe/H] < −1 stars by Fuhrmann (2008, 2011) from the LTE analysis. Adibekyan et al. (2012) derived the LTE abundances of a large sample of nearby stars, and using Mg, Si, and Ti as representatives of the α-process elements, they

concluded that the α-enhancement for the thick disk and the stars with [Fe/H] < −0.5 is close to 0.3 dex.

Odd-Z elements. We consider Na and Al together, although conclusions related to Al are less firm due to lower accuracy of the derived Al abundances, as discussed in Section 4.1. Both Na and Al follow the Fe abundance in the thin- and thick-disk stars (Figure 10). In most halo stars the Na/Fe and Al/Fe ratios are subsolar, with a rather large scatter of data. In contrast, a well-defined downward trend is observed for Na/Mg, when [Fe/H] decreases from supersolar values to −1, and the more MP stars form a plateau at [Na/Mg] ≃ −0.5 (Figure 11). The Na/Al ratios seem to be solar, independent of metallicity. The two halo stars, HD 74000 and G090-003, are clear outliers, with [Na/Fe] ⩾ 0.2 and [Na/Mg] ≃ 0. The latter (G090-003) has also high [Al/Fe] = 0.27, but normal Na/Al. See notes on these two stars in Section 4.3. One more star, HD 108177, has higher [Na/Fe] = 0.04 and [Na/Mg] = −0.15 compared with the halo stars of similar metallicity.

A metal-poor plateau for Na/Mg was reported in the earlier NLTE studies by Gehren et al. (2006), with [Na/Mg] = −0.7 for the −3.1 ⩽ [Fe/H] < −1.8 dwarfs, and Andrievsky et al. (2010), with [Na/Mg] ≃ −0.8 for the −4.2 ⩽ [Fe/H] < −2 giants. The difference between our value, [Na/Mg] ≃ −0.5, and the literature data is, most probably, due to overestimated magnesium NLTE abundances in Gehren et al. (2006) and Andrievsky et al. (2010). For example, the latter paper reported a mean [Mg/Fe] = 0.61 for their stellar sample, while, in this study, an MP plateau was obtained at [Mg/Fe] = 0.28. The difference in Mg abundances is, in turn, probably due to different treatment of inelastic collisions with H I atoms. Our study takes advantage of employing the Mg I + H I collision rates from quantum mechanical calculations of Barklem et al. (2012), while Gehren et al. (2006) and Andrievsky et al. (2010)
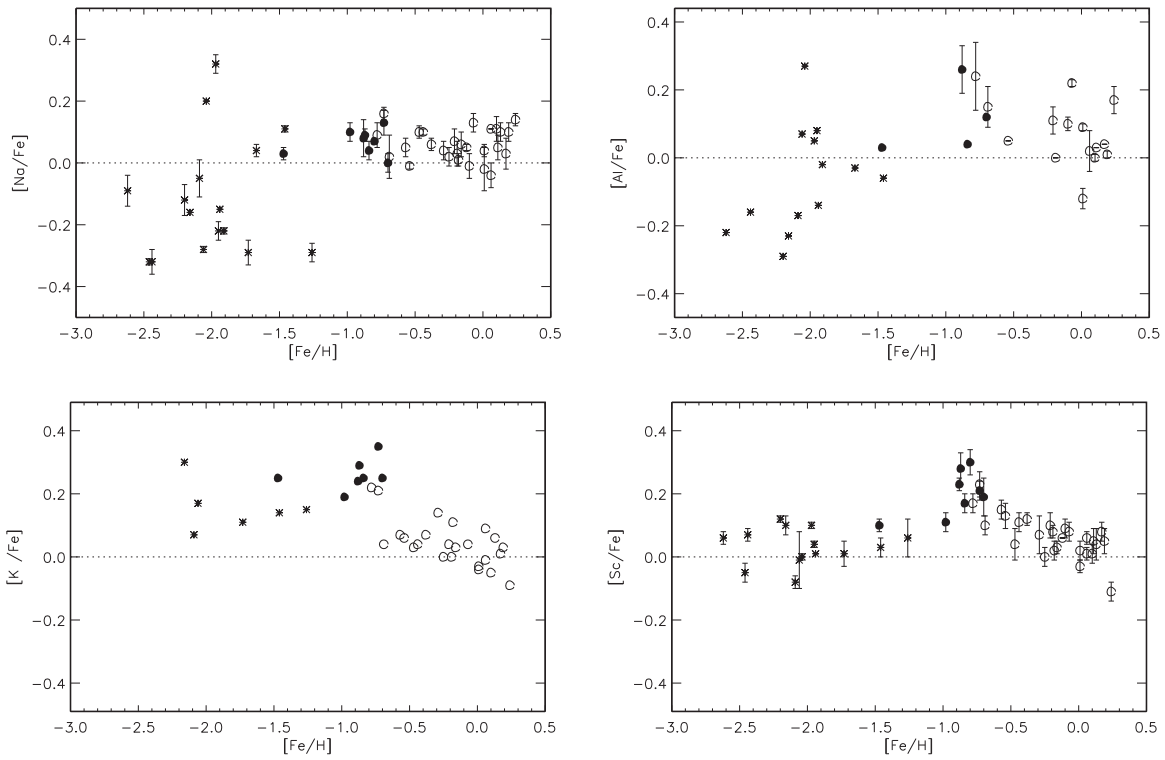
Figure 10. Same as in Figure 8, but for the odd-Z elements Na, Al, K, and Sc.
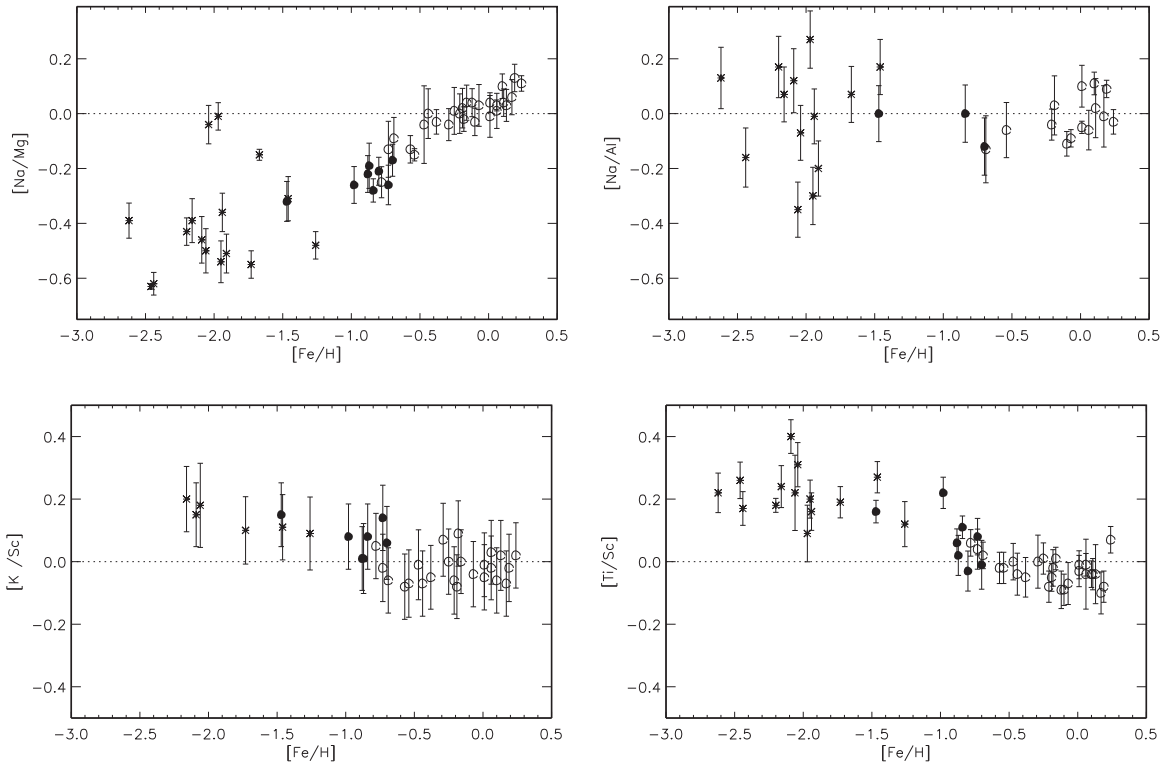
Figure 11. Stellar NLTE abundance ratios involving the odd-Z elements. The same symbols are used as in Figure 7.

used the formula of Steenbock & Holweger (1984) with $S_H = 0.05$ and 1/3, respectively.

The heavier odd-Z elements, K and Sc, behave like the α-elements in the thin- and thick-disk stars, at [Fe/H] > −1 (Figure 10). Indeed, K/Fe and Sc/Fe grow toward lower

metallicity from the solar value to [K/Fe] ≃ 0.25 and [Sc/Fe] ≃ 0.2. In the halo stars, potassium remains to be enhanced relative to Fe, but with the lower magnitude, [K/Fe] < 0.2, while Sc/Fe is close to the solar value. As a result, the trends are nonmonotonous, and a group of the
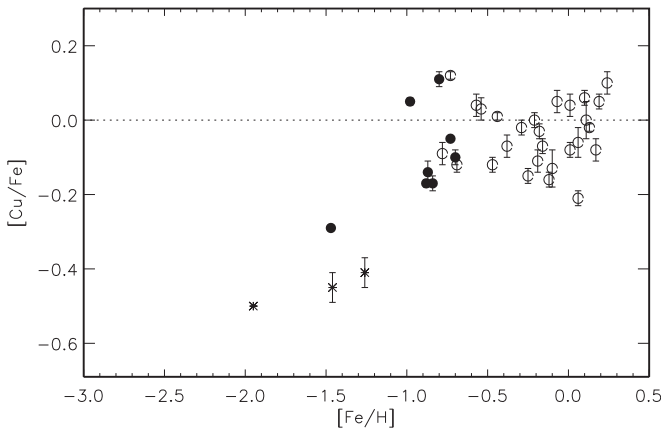
Figure 12. Same as Figure 8, but for copper.

thick-disk stars at [Fe/H] around -0.8 looks like a local peak. In contrast, the K/Sc, Ca/Sc, and Ti/Sc ratios reveal a remarkably monotonous behavior, with a rather small scatter of data for stars of similar metallicity (see [K/Sc] and [Ti/Sc] in Figure 11). This suggests a common site of the K–Ti production.

Copper. The thin- and thick-disk stars with [Fe/H] $\geqslant -1$ reveal very similar and close-to-solar Cu/Fe ratios (Figure 12). The statistics are very poor at the lower metallicity, where we could measure the Cu abundances for three halo stars and the thick-disk star HD 94028. Copper is underabundant relative to Fe in all four stars, with [Cu/Fe] between -0.41 and -0.50 in the halo stars and a slightly higher value of -0.29 in HD 94028. Our data, combined with the three $-1.3 <$ [Fe/H] < -1 stars from Yan et al. (2015), suggest an upward trend, where [Cu/Fe] increases from -0.5 at [Fe/H] $\simeq -2$ to about -0.1 at [Fe/H] $\simeq -0.8$.

Neutron-capture elements: Sr, Zr, Ba, and Eu. Here, we concentrate mostly on the $-2.2 \leqslant$ [Fe/H] $\leqslant +0.24$ metallicity range. For none of the three stars at the lower metallicity was their Eu abundance measured, and a big scatter was obtained for Sr/Fe, Zr/Fe, Ba/Fe (Figure 13), and the ratios among the neutron-capture elements (Figure 14). One of these stars is a well-studied *r*-process-poor star HD 140283 (see Siqueira-Mello et al. 2015, and references therein) that is strongly underabundant in Sr and Ba relative to Fe and has an ~0.4 dex lower Zr/Fe ratio compared with that for the remaining halo stars. In our most MP star, BD $-13°3442$ ([Fe/H] $= -2.62$), abundances of only Sr and Ba were determined, and their ratio deviates strongly from Sr/Ba of the remaining stellar sample. In the $-2.2 \leqslant$ [Fe/H] $\leqslant +0.24$ stars Sr and Ba follow the Fe abundance, although with a substantial scatter of ± 0.2 dex. It is worth noting that similar scatter for Ba/Fe was also obtained in the earlier studies (e.g., Edvardsson et al. 1993; Mashonkina et al. 2003; Bensby et al. 2014). Europium is enhanced relative to Fe in the [Fe/H] < -1 stars, with mean [Eu/Fe] $\simeq 0.5$, and a downward trend of Eu/Fe, with a rather small scatter of data, is observed at the higher metallicities. Such a behavior is typical of the *r*-process elements, and the knee at [Fe/H] $\simeq -1$ indicates the onset of the Fe production by Type Ia SNe (SNe Ia). A very similar behavior can be seen in Figure 13 for Zr/Fe, although the thin-disk stars reveal a less pronounced upward trend compared with that for Eu/Fe.

As seen in Figure 14, the ratios among Sr, Zr, Ba, and Eu reveal the well-defined Galactic trends, with a rather small scatter of data for stars of similar metallicity. Barium follows the Sr abundance, suggesting their common origin during the period when the Fe abundance of the Galactic matter grew from [Fe/H] $\simeq -2.5$ to the modern value. In the solar system matter 80% of barium and 80% of strontium were produced in the slow (*s*) process of neutron-capture nuclear reactions (Travaglio et al. 1999, 2004). For Ba, this is exclusively the main *s*-process occurring in intermediate-mass stars of 1–4 $M_\odot$ during the asymptotic giant branch (AGB) phase, while 9% of solar Sr originates from the weak *s*-process occurring in the helium-burning core phase of massive stars ($M > 10$ $M_\odot$). The remaining solar Ba originates from the rapid (*r*) process. Astrophysical sites for the *r*-process are still debated, although they are likely associated with explosions of massive stars, with $M > 8$ $M_\odot$. Analysis of Sr, Y, and Zr in the *r*-process-enhanced stars and extremely MP ([Fe/H] < -3) stars led Travaglio et al. (2004) to suggest the lighter-element primary process (LEPP) that in the early Galaxy contributed to the light neutron-capture elements, but not to the heavy ones, beyond Ba. Travaglio et al. (2004) estimated empirically the LEPP contribution to solar Sr as 8%. Based on our data for stellar Sr/Ba, we infer that, if it existed, the LEPP contribution to galactic Sr did not change during the $-2.5 <$ [Fe/H] $\leqslant +0.24$ epoch.

Europium is enhanced relative to Ba in our halo and thick-disk stars, with a scatter of [Eu/Ba] between 0.31 and 0.82. The mean is [Eu/Ba] $= 0.50 \pm 0.14$. As discussed, a halo star HD 74000 is an outlier, and it was not included in the mean. The thin-disk stars reveal the upward trend in Eu/Ba toward lower metallicity. Europium is referred to as an *r*-process element, because only 6% of solar Eu originates from the *s*-process (Travaglio et al. 1999). Theoretical predictions of a pure *r*-process production of Eu and Ba give [Eu/Ba]$_r \simeq 0.67$ in the classical waiting-point (WP) approximation (Kratz et al. 2007) and [Eu/Ba]$_r \simeq 0.87$ in the large-scale parameterized dynamical network calculations of Farouqi et al. (2010) in the context of an adiabatically expanding high-entropy wind, as is expected to occur in core-collapse SNe. The solar *r*-residual, i.e., the difference between solar total and *s*-abundance, where the *s*-abundance is deduced from the Galactic chemical evolution models, ranges between [Eu/Ba]$_r = 0.71$ (Travaglio et al. 1999) and 0.80 (Bisterzo et al. 2014). Our data on Eu/Ba (top right panel in Figure 14) provide evidence for a dominant contribution of the *r*-process to the production of Ba and Eu in the early Galaxy, when the halo and thick-disk stellar population formed, and rapidly growing enrichment of the Galactic matter by *s*-nuclei, when metallicity increased from [Fe/H] $\simeq -0.8$ to the solar value.

A behavior similar to that for Eu/Ba is observed also for Zr/Ba, although an enhancement of Zr relative to Ba in the halo and thick-disk stars is, on average, smaller, if not counting the two most MP stars. According to Travaglio et al. (2004), 67% of the solar Zr was contributed by the main and weak *s*-process, and 15% and 18% was attributed to the *r*- and LEPP-process, respectively. Considering contributions from the *r*- and LEPP-process together, we deduce the solar *r*-residual [Zr/Ba]$_r \simeq 0.22$. This is smaller than the [Zr/Ba] observed in the halo and thick-disk stars. As expected, the Zr/Sr ratio is close to the solar value in the thin-disk stars, but it grows steeply in the thick-disk and halo stars,
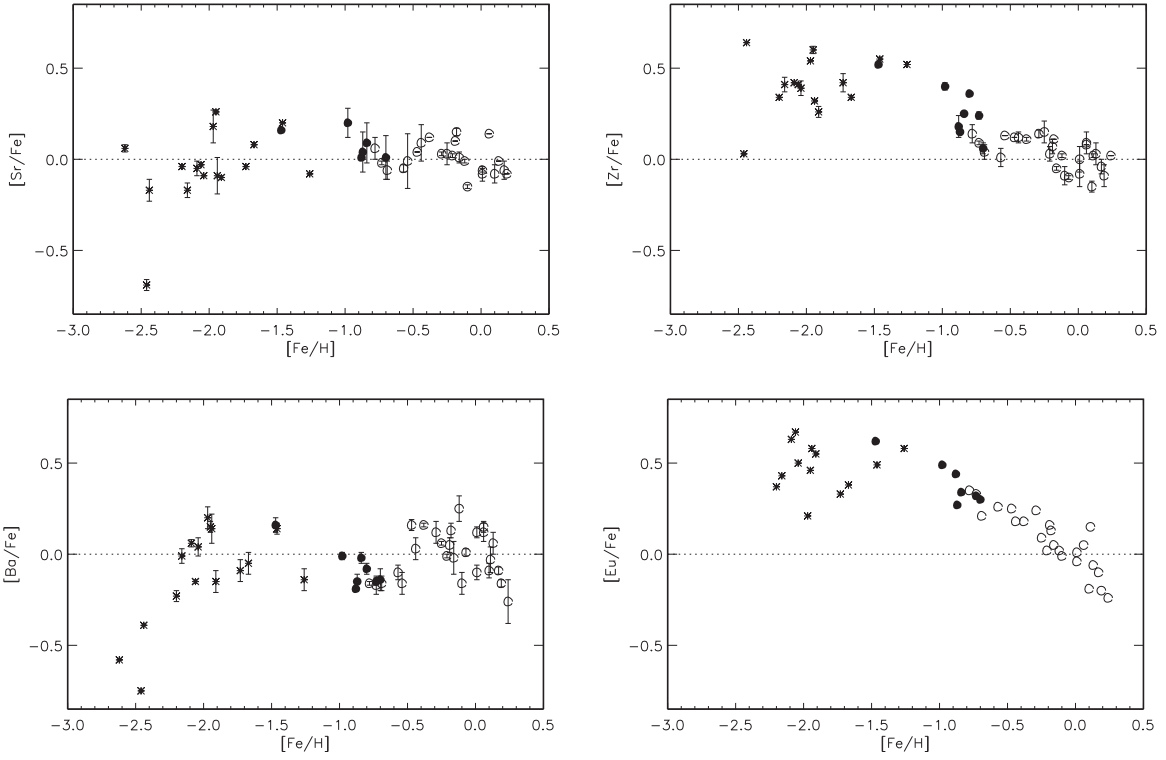
Figure 13. Same as Figure 8, but for the neutron-capture elements Sr, Zr, Ba, and Eu.
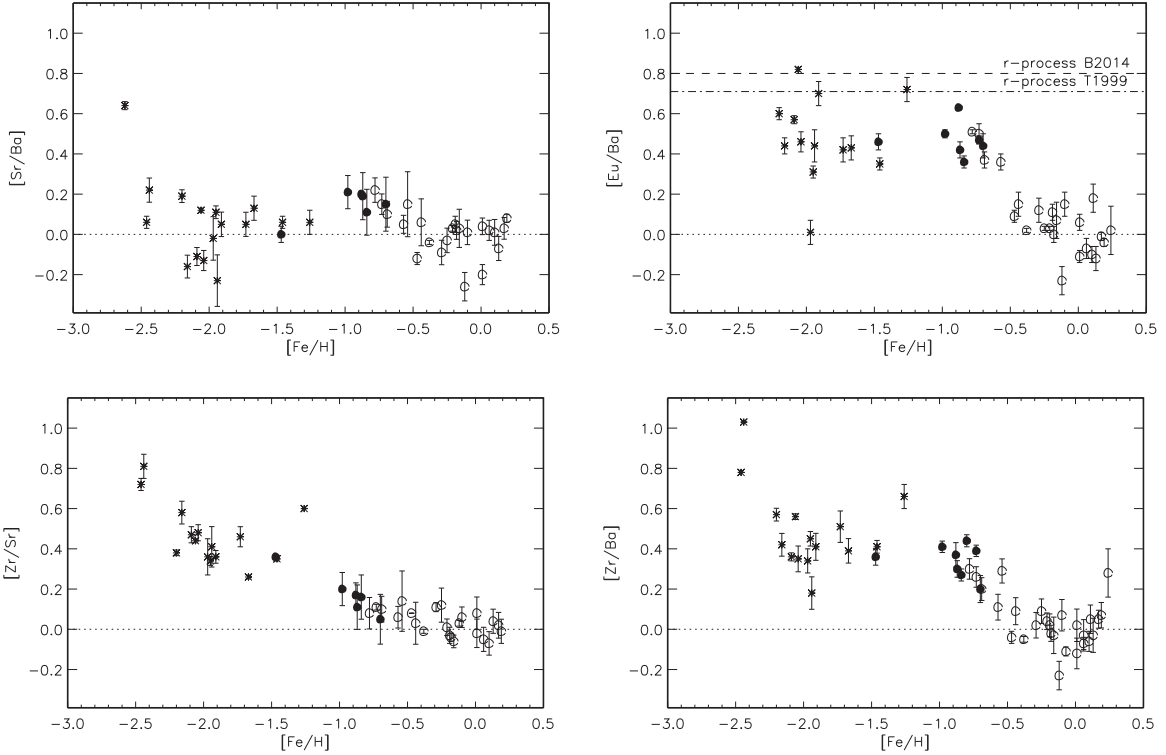

Figure 14. Stellar NLTE abundance ratios between the neutron-capture elements. The same symbols are used as in Figure 7. The dashed and dot-dashed lines indicate the ratios corresponding to the solar r-residuals, as predicted by GCE calculations of Bisterzo et al. (2014) and Travaglio et al. (1999), respectively.

approaching $[Zr/Sr] \simeq 0.8$ at $[Fe/H] = -2.5$. Using predictions of Travaglio et al. (2004), we deduced $[Zr/Sr]_{r+LEPP} = 0.22$ and $[Zr/Sr]_{LEPP} = 0.35$ for production of Sr and Zr in the r- and LEPP-process together and in a pure LEPP-process. An origin of Zr in the thick-disk stars can be attributed to

these two processes. However, further efforts should be invested to understand high Zr/Sr ratios observed in the $[Fe/H] < -2$ stars.

Obtained abundances of Sr, Zr, Ba, and Eu support, in general, the literature data in the metallicity range overlapping

with ours, despite the fact that most studies were performed under the LTE assumption. This is because the NLTE abundance corrections for lines of Sr II, Zr II, and Eu II are small in the stellar parameter range, with which we are concerned (see Section 3.3). The upward trend in [Zr/Fe] was reported by Mashonkina et al. (2007b) and Mishenina et al. (2013), although the latter paper studied a narrow range of metallicity, down to [Fe/H] $\simeq -1$. Enhancement of Eu relative to Fe and Ba in the halo and/or thick-disk stars was obtained earlier by Mashonkina & Gehren (2000), Burris et al. (2000), Barklem et al. (2005), Bensby et al. (2005), and Mishenina et al. (2013). With a different stellar sample, Mashonkina et al. (2007b) found Galactic trends for Zr/Ba and Zr/Sr that are very similar to ours.

5.2. Influence of NLTE on the Galactic Abundance Trends

As noted, this study employs a line-by-line differential analysis with respect to the Sun. Here, we discuss the impact of NLTE on determination of the mean element abundances [X/H] and elemental ratios, depending on the star's metallicity. Figure 15 displays the differences between the NLTE and LTE [X/H] ratio for the 14 investigated species. We do not show the data for Li I (see Figure 2 for the NLTE effects), Ti II (due to minor differences), and Fe I–Fe II, which were discussed in Paper I.

A differential approach largely cancels the (NLTE–LTE) differences in [X/H] for most species in the [Fe/H] > -1 stars, even if the departures from LTE for individual lines are large. This concerns, in particular, [C/H], [Na/H], [Ca/H], and [Ba/H]. For example, Δ_{NLTE} for lines of C I can be up to -0.4, while the [C/H] differences between the NLTE and LTE do not exceed 0.1 dex in absolute value. However, notable (>0.1 dex) differences between NLTE and LTE in the [Fe/H] > -1 stars remain for [O/H] and [K/H]. It is worth noting that NLTE can also affect the [Eu/Ba] ratios because the differences between NLTE and LTE are negative for [Ba/H] but positive for [Eu/H]. An advantage of NLTE is also proved by the smaller line-to-line scatter obtained for most species and most stars in NLTE compared with LTE (see Table 3). For example, for HD 49933 (6600/4.15/-0.47) LTE leads to [O/H] $= -0.15 \pm 0.11$, [Ca/H] $= -0.37 \pm 0.08$, and [Ba/H] $= -0.22 \pm 0.13$, while remarkably smaller statistical errors are obtained in NLTE, with [O/H] $= -0.37 \pm 0.04$, [Ca/H] $= -0.43 \pm 0.04$, and [Ba/H] $= -0.31 \pm 0.03$.

NLTE is a major step forward for studies of stars more metal-poor than [Fe/H] $= -1$. The (NLTE–LTE) differences in [X/H] grow in absolute value toward lower metallicity and, for most species, can reach 0.2 dex and even more. Exceptions are [Mg/H], [Si/H], [K/H], [Zr/H], and [Eu/H], where the departures from LTE are small. NLTE is, in particular, important for elemental ratios involving the species with (NLTE–LTE) of different sign, like [Na/Mg], [Na/Al], [Na/Cu], and [Sr/Ba]. For example, the mean for the halo stars, excluding HD 74000 and G090-003, amounts to [Na/Mg] $= -0.47 \pm 0.10$ in NLTE and -0.25 ± 0.19 in LTE. NLTE makes the Al abundance following the Na one over the whole metallicity range under investigation, with the mean [Na/Al] $= -0.01 \pm 0.14$, while LTE finds a large overabundance of Na relative to Al in the halo and thick-disk stars ([Na/Al] $= 0.58 \pm 0.38$) and close-to-solar Na/Al ratios in the thin-disk stars.

5.3. Comparison with the Galactic Chemical Evolution Models

In this section, we compare our observational data with a series of GCE models from the literature. We will mainly discuss the models of K11 (Kobayashi et al. 2011b) and its updated version, K15. Their main features include slow infall, no outflow, star formation proportional to gas fraction, the Kroupa (2001) initial mass function (IMF) at 0.01–50 $M_\odot$, and the SN Ia model based on the single-degenerate scenario (Kobayashi & Nomoto 2009) with the metallicity effect (Kobayashi et al. 1998). The metallicity-dependent nucleosynthesis yields are taken from Kobayashi et al. (2006, hereafter K06) and Kobayashi et al. (2011b) for SNe and hypernovae (with a 0.5 fraction of hypernovae at $\geqslant 20\, M_\odot$), and from Karakas (2010) for AGB stars. The yield sets are identical to those in Nomoto et al. (2013). Further, in the K15 model, the effect of 2D jet-like explosions is applied (see Sneden et al. 2016, for the details). These GCE results are consistent with the metallicity distribution function, the present star formation rate, and the present gas fraction.

Besides K11 and K15, we also compared our results with other widely used GCE models from Chiappini et al. (1997, hereafter C97), Samland (1998, hereafter S98), Goswami & Prantzos (2000, hereafter GP00), François et al. (2004, hereafter F04), and Romano et al. (2010, hereafter R10). C97 presented a model that assumes two main infall episodes that formed the halo/thick disk and the thin disk, respectively. S98 developed a chemodynamical model of an isolated disk galaxy to be consistent with the observations deriving empirical yields. The model takes into account the galactic dynamical process for various kinds of stars and ISM. GP00 described an independently evolved halo+disk model, with short-timescale outflows for the halo and slow infall of the disk. F04 also presented a two-infall model that is similar to C97, but with empirical stellar yields. R10 tested 15 GCE models with various sets of stellar yields from the literature. Figures 16 and 17 show the comparison between our observational data and the predictions from those GCE models. The offsets of solar abundances from different works have been corrected.

Carbon—The [C/Fe] ratio predicted by K11 and K15 shows a waved line, which slightly decreases from [Fe/H] ~ -3 to -1.7, due to the smaller envelope mass that contains C of massive progenitor stars. The rapid increase from [Fe/H] ~ -1.5 to -1 is caused by the delayed enrichment from AGB stars with $\sim$1–4 $M_\odot$. From [Fe/H] ~ -1, [C/Fe] decreases due to the delayed enrichment of SNe Ia. Although the lifetimes of these AGB stars (0.15–0.2 Gyr) are comparable to the shortest lifetimes of SNe Ia, the SN Ia contribution appears after the AGB contribution because of the metallicity dependence of the SN Ia lifetimes (Kobayashi et al. 1998; Kobayashi & Nomoto 2009). These trends are characteristic of K11 and K15 models and are in excellent agreement with our observational data at [Fe/H] $\gtrsim -1.5$. At [Fe/H] $\lesssim -1.5$, the models predict $\sim$0.1–0.2 dex lower [C/Fe]. This is due to the input C yields, and this amount of offset can easily be solved with normal rotation of stars or the convective mixing of hydrogen into the He-burning layer (without rotation). The waved line can be also seen in model 15 of R10.

Oxygen—The observed [O/Fe] trend is in good agreement with the K11 and K15 models, where the plateau at [O/Fe] ~ 0.6 is caused by core-collapse SNe, while the decreasing trend from [Fe/H] ~ -1 is caused by SNe Ia.
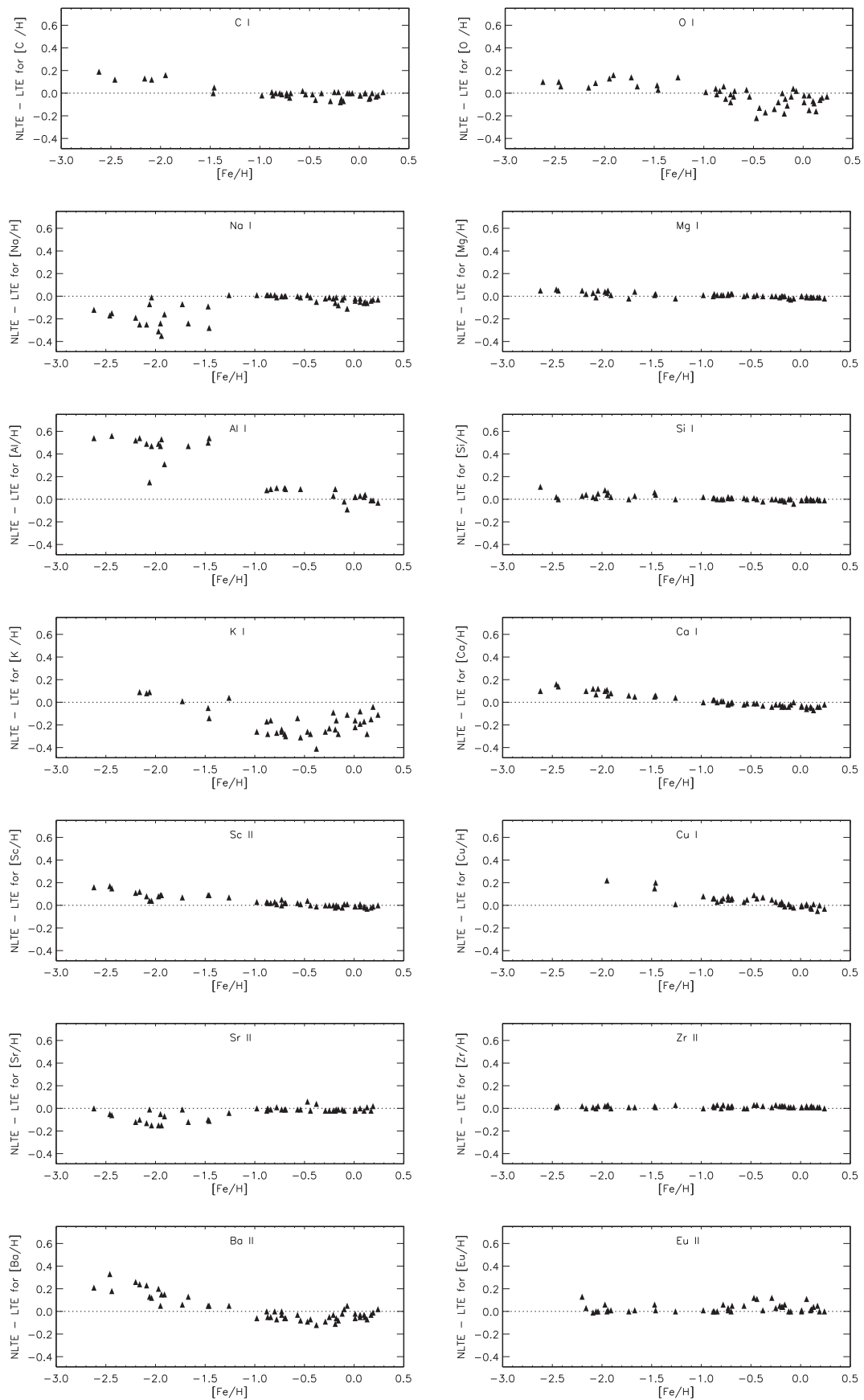
Figure 15. Differences in differential abundance [X/H] between NLTE and LTE for the investigated sample.
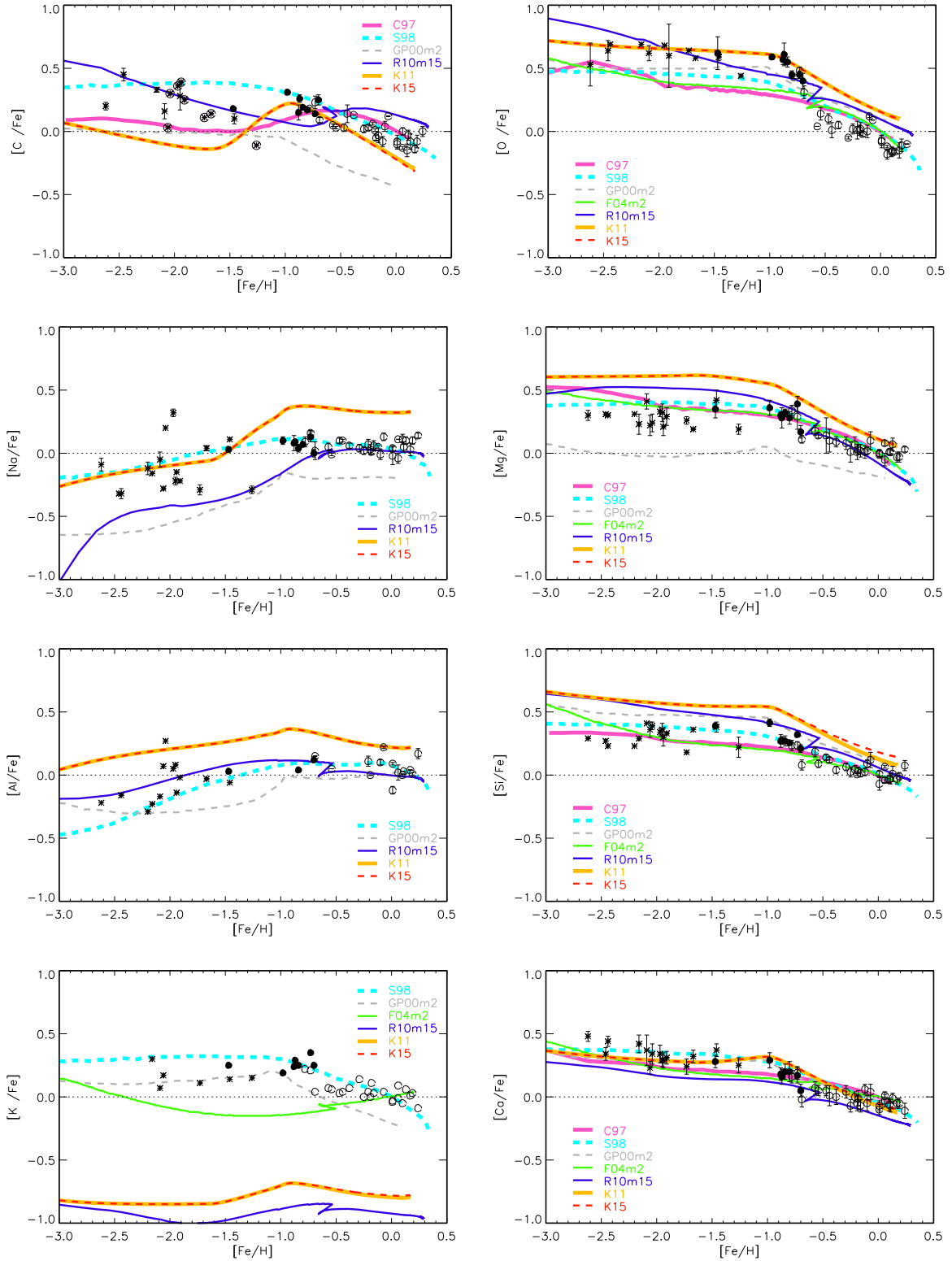
Figure 16. Comparison with the Galactic chemical evolution models. The models used in the figure are C97 (violet solid line), S98 (turquoise dashed line), GP00m2 (gray dashed line), F04m2 (green solid line), R10m15 (blue solid line), K11 (orange solid line), and K15 (red dashed line), where GP00m2, F04m2, and R10m15 represent the model of "thick curve" in GP00, the model of Figures 4–6 in F04, and model 15 in R10, respectively.

This trend should exist for all α elements, i.e., O, Mg, Si, S, and Ca. It is very important that this evolutionary change appears sharply, and there are no stars with [O/Fe] $\lesssim 0.5$ at [Fe/H] $= -1$. As in Figure 6 of K11, without the metallicity effect of SNe Ia, the evolutionary change occurs much more gradually, which is inconsistent with our new observational

data. Other models did not show the sharp change at [Fe/H] $= -1$.

Sodium—In the K11 and K15 models, Na production highly depends on the metallicity of progenitors of core-collapse SNe, which causes the increasing trend from [Fe/H] ~ -3 to ~ -1.5. This agrees with the observational data very well.
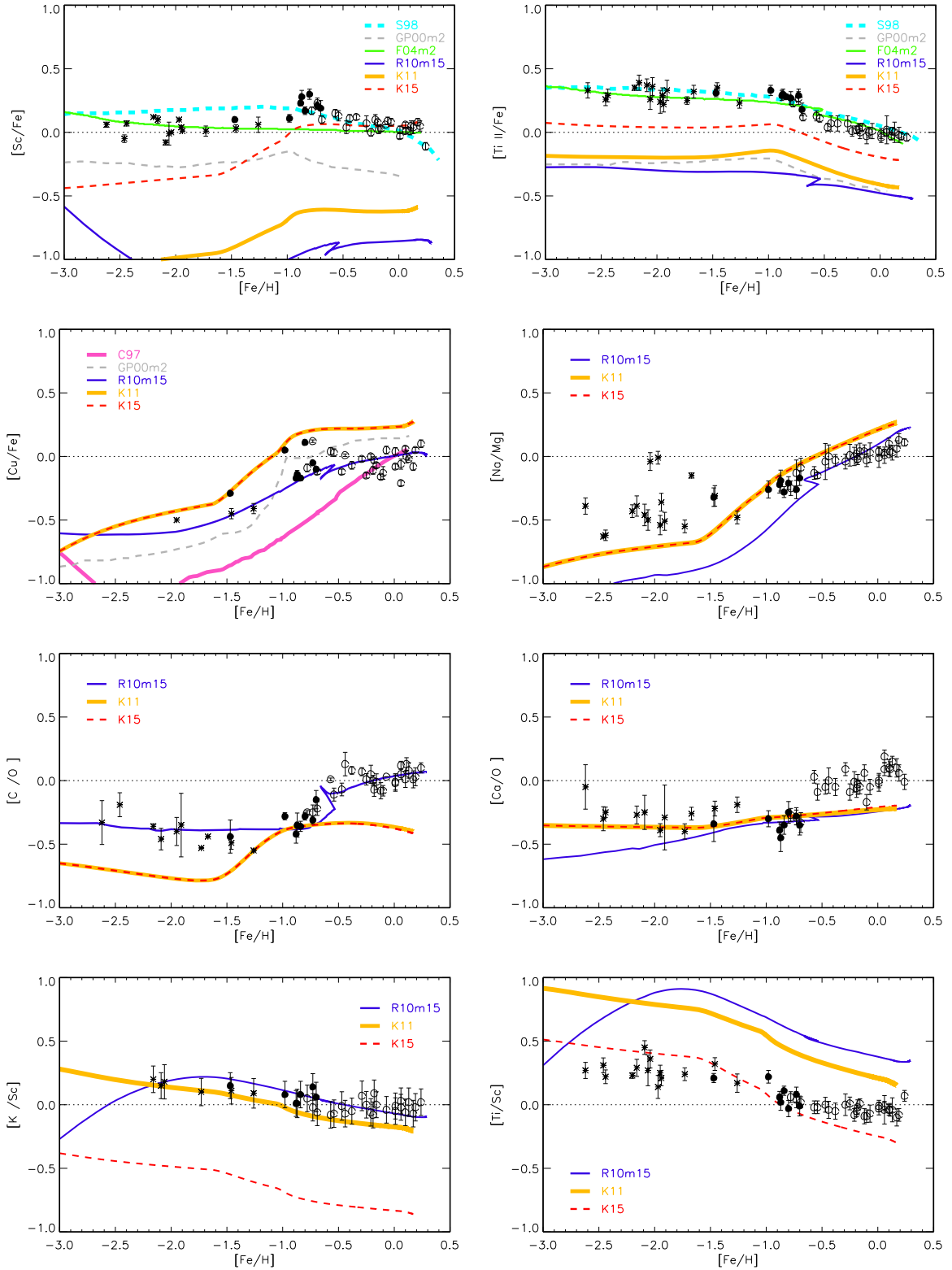
Figure 17. Comparison with the Galactic chemical evolution models. The colors are the same as in Figure 16.

From [Fe/H] ∼ −1.5, [Na/Fe] ratios increase quickly due to AGB stars. Note that with the updated reaction rates, the Na yields of AGB stars have been reduced. However, Na is still overproduced by AGB stars. S98 may predict a better trend, but it uses empirical yields that are determined from the observations.

Magnesium—The observed [Mg/Fe] ratios show the same trend as [O/Fe], but there is a ∼0.25 dex offset between the

observations and K11/K15 models. This means that [O/Mg] is not zero at a wide range of metallicity. This could be partially solved with the mass dependence of core-collapse SNe, where [O/Mg] is slightly higher for more massive SNe (≳30 $M_\odot$; see Figures 1–4 of K06). This could also be solved by uncertain reaction rates in the hydrostatic burning of progenitor stars, as shown in Figure 9 of K06. Note that O and Mg are synthesized

roughly in the same region of SN ejecta, and hence [O/Mg] should not depend on the parameters of SN explosions very much. The Mg production of AGB stars is negligible in GCE models (except for the isotopic ratios; K11).

Aluminum—Similar to Na, the trend predicted by K11 and K15 is consistent with the observational data, but similar to Mg, there is a ~0.25 dex offset. These could be due to the reaction rates, the rotational/convective mixing, or a combination of both. The trend predicted by model 15 of R10 is in good agreement with the observation.

Silicon—Similar to Mg, the observed trend is well reproduced with the K11 and K15 models, but the model is ~0.2–0.3 dex higher than observed. Si yields depend on the progenitor mass and the explosion energy of core-collapse SNe, so some combination of these could reduce [Si/O] ratios. Note that if there is pre-enrichment from pair-instability SNe, which should occur if 140–300 $M_\odot$ stars exist, the [Si/Fe] ratios become much higher, which is inconsistent with the observations (e.g., Cayrel et al. 2004).

Potassium—The underproduction of K in K11 and K15 is, at least partially, due to the lack of a neutrino process (Kobayashi et al. 2011a). This element has not been well studied before because of the uncertainty of the NLTE effect, but our observational data can give strong constraints on SN nucleosynthesis. Similar underproduction of K is seen in model 15 of R10.

Calcium—Similar to [O/Fe], the K11 and K15 models excellently reproduce the observed [Ca/Fe] ratios, and the sharp evolutionary change at [Fe/H] = −1 strongly supports the metallicity effect of SNe Ia.

Scandium—In K15 the Sc abundance can be increased by the 2D jet-like explosions (Maeda & Nomoto 2003), as shown in Figure 17 by the dashed lines. This could also be enhanced by the neutrino process as for K. It is worth noting that all the models except S98 failed to reproduce the observed [Sc/Fe] trend in the whole metallicity range.

Titanium—This is the long-standing Ti problem in GCE, where the predicted [Ti/Fe] ratios are much lower than observed. The 2D jet effect should increase Ti abundances (dashed lines in Figure 17), but this may not be enough to solve this problem. Ti is produced in almost the same region as Fe in SN ejecta, and hence it is categorized not as an α-element but as an iron-peak element. Nucleosynthesis with multidimensional explosions is necessary to understand the Ti production.

Copper—The trends predicted by K11 and K15 models are similar to those observed, although the model is a bit higher at [Fe/H] > −1.0. This is caused by the star formation rates connected with IMF. [Cu/Fe] increases toward higher metallicity because Cu is an odd-Z element, the production of which depends on the progenitor metallicity. This agreement suggests that the main producer of Cu is core-collapse SNe, not the weak slow neutron-capture process suggested by Pignatari et al. (2010).

Without normalization with respect to Fe, it may be possible to constrain uncertain processes that are important for some specific elements. The [Na/Mg] ratio in Figure 17 implies that the metallicity dependence may be smaller than those in K11 and K15. The [C/O] ratio may suggest that the mixing and/or rotation may be more important than those in K11 and K15. Note that in model 15 of R10 the C yields in stellar winds are added, but a part of these have already been included in SN yields, so the high [C/O] ratio should be due to the double

count of C production. In K15, the [Ca/O] ratios are consistent with the observed ones at [Fe/H] $\lesssim$ −0.5, but are lower at higher metallicity, which may be due to the contribution to observed Ca from SNe Ia. [K/Sc] and [Ti/Sc] are in particular interesting since [(K, Sc, Ti)/Fe] is underabundant in K11. The low [K/Sc] may suggest the importance of the ν-process, and the [Ti/Sc] ratio supports the 2D effect applied in K15 to some extent. These figures should be used to test the next generation of nucleosynthesis yields with multidimensional calculations.

6. CONCLUSIONS

Using accurate atmospheric parameters determined in Paper I and high-resolution ($R \simeq 60,000$) stellar spectra observed for our project with the Shane/Hamilton spectrograph (the Lick Observatory) and also taken from the archives, we calculated the NLTE abundances for 17 elements in a sample of stars uniformly distributed over the −2.62 $\leqslant$ [Fe/H] $\leqslant$ +0.24 metallicity range. The star sample has been kinematically selected to trace the Galactic thin and thick disks and halo. This is the first extensive NLTE study of the stellar sample suitable for the Galactic chemical evolution research.

We derive differential abundances relative to the Sun, and such an approach largely cancels the difference between NLTE and LTE for [C/H], [Na/H], [Ca/H], and [Ba/H] for the [Fe/H] > −1.0 stars. However, notable (>0.1 dex) differences in the same stars were found for [O/H], [K/H], and [Eu/Ba]. The advantage of NLTE is proved by the smaller line-to-line scatter obtained for most species in most stars in NLTE compared with that for LTE. The (NLTE–LTE) abundance differences grow toward lower metallicity, and NLTE is essential for stars more metal-poor than [Fe/H] = −1, in particular, for elemental ratios involving the species with (NLTE–LTE) of different sign, like [Na/Mg], [Na/Al], [Na/Cu], and [Sr/Ba].

In line with the earlier studies, we obtained that the halo dwarf stars, which are expected to keep the pristine Li abundance, reveal a clear temperature dependence of their Li abundance. In our warm ($T_{\rm eff} \geqslant 5800$ K) stars, the mean is $\log \varepsilon_{\rm Li} = 2.2$, which is consistent with $\log \varepsilon_{\rm Li} = 2.177 \pm 0.071$ deduced by Charbonnel & Primas (2005) for the [Fe/H] $\leqslant$ −1.5 stars with $T_{\rm eff} \geqslant 5700$ K. Further theoretical studies of stellar physics and evolution are needed to understand source(s) of discrepancy with the standard BBN that predicts $\log \varepsilon_{\rm Li} = 2.72 \pm 0.06$ (Coc et al. 2012) and discrepancy between the warm and cool ($T_{\rm eff} < 5800$ K) halo dwarf stars.

Most Galactic abundance trends obtained for elements of stellar origin have a rather small scatter of data for stars of similar metallicity. It was found that the element-to-iron ratios reveal a common behavior for O, Mg, Si, Ca, and Ti, with an MP plateau, a knee at [Fe/H] $\simeq$ −0.8, and a downward trend for higher metallicity. In the halo and thick-disk stars [O/Fe] = 0.61 and a 0.3 dex lower [X/Fe] ratio was obtained for Mg, Si, Ca, and Ti. An upward trend of [C/Fe] with decreasing metallicity is observed in the thin-disk stars, and a very similar value of [C/Fe] = 0.21 is observed in the thick-disk stars. In contrast to [C/Fe], which reveals a substantial scatter in the halo stars, a well-defined trend was obtained for the C/O ratios, with the upturn at [Fe/H] $\simeq$ −1.2, in line with the earlier finding of Akerman et al. (2004). We obtained no systematic shift between the NLTE abundances from lines of C I and the

CH-based abundances over the entire metallicity range under investigation.

A rather large scatter of data is observed when comparing abundances of the odd-Z elements Na, K, and Sc with iron; however, it is largely removed in the ratios between these elements, like K/Sc, and in the ratios between nearby odd-Z and even-Z elements, like Na/Mg and Sc/Ti, suggesting a common production site for Na to Ti. We find a nearly constant underabundance of Na relative to Mg in the $[\mathrm{Fe/H}] < -1$ stars, with the mean $[\mathrm{Na/Mg}] \simeq -0.5$.

The light neutron-capture elements Sr and Zr reveal a different behavior, namely, Sr follows the Fe abundance down to $[\mathrm{Fe/H}] \simeq -2.5$, but Zr is enhanced relative to Fe and Sr in the MP stars. The [Zr/Sr] ratio is close to the solar value in the thin-disk stars, grows to 0.4 at $[\mathrm{Fe/H}] = -2$, and approaches 0.8 at $[\mathrm{Fe/H}] = -2.5$. In line with earlier studies, the upward trend in [Eu/Fe] exists for $[\mathrm{Fe/H}] > -1$, and europium is enhanced relative to Fe by more than 0.3 dex in the halo stars. A plateau of [Eu/Ba] at 0.50 is formed by the halo and thick-disk stars, the knee occurs at $[\mathrm{Fe/H}] \simeq -0.8$, and the downward trend in [Eu/Ba] is observed for higher metallicities.

The use of the NLTE element abundances gives increased credit to the interpretation of the data in the context of the chemical evolution of the Galaxy. Although GCE models are not calibrated with our NLTE abundances in this paper, K15 model predictions are in good agreement for C, O, Ca, and Fe in some metallicity coverages and the overall shapes. The underproduction of K, Sc, and Ti is somewhat known and is due to the lack of ν-processes (Sneden et al. 2016). The offsets in odd-Z elements (i.e., Na, Al, Cu) give important constraints on uncertain processes such as mixing. Despite the agreement for O, the offsets for Mg may be the most problematic since both elements have formed in the relatively robust stellar evolution phase. If [Mg/Fe] is as low as in our NLTE analysis, that requires a different C/O ratio due to the mixing, mass-loss, and/or reaction rates in the progenitor stars, which should be studied in future works.

Software: DETAIL (Butler & Giddings 1985), SIU (Reetz 1991), synthV-NLTE (Ryabchikova et al. 2016), bin-mag3 (http://www.astro.uu.se/ oleg/download.html).

REFERENCES

Adibekyan, V. Z., Sousa, S. G., Santos, N. C., et al. 2012, A&A, 545, A32
Akerman, C. J., Carigi, L., Nissen, P. E., Pettini, M., & Asplund, M. 2004, A&A, 414, 931
Alexeeva, S. A., & Mashonkina, L. I. 2015, MNRAS, 453, 1619
Allende Prieto, C., Barklem, P. S., Lambert, D. L., & Cunha, K. 2004, A&A, 420, 183
Amarsi, A. M., Asplund, M., Collet, R., & Leenaarts, J. 2015, MNRAS, 454, L11
Andrievsky, S. M., Spite, M., Korotin, S. A., et al. 2010, A&A, 509, A88
Bagnulo, S., Jehin, E., Ledoux, C., et al. 2003, Msngr, 114, 10
Barklem, P. S., Belyaev, A. K., Spielfiedel, A., Guitou, M., & Feautrier, N. 2012, A&A, 541, A80
Barklem, P. S., Christlieb, N., Beers, T. C., et al. 2005, A&A, 439, 129
Barklem, P. S., & O'Mara, B. J. 1998, MNRAS, 300, 863
Barklem, P. S., Piskunov, N., & O'Mara, B. J. 2000, A&AS, 142, 467
Baumueller, D., & Gehren, T. 1996, A&A, 307, 961
Bautista, M. A., Gull, T. R., Ishibashi, K., Hartman, H., & Davidson, K. 2002, MNRAS, 331, 875
Belyaev, A. K. 2013, A&A, 560, A60
Belyaev, A. K., & Barklem, P. S. 2003, PhRvA, 68, 062703
Belyaev, A. K., Yakovleva, S. A., & Barklem, P. S. 2014, A&A, 572, A103
Bensby, T., Feltzing, S., Lundström, I., & Ilyin, I. 2005, A&A, 433, 185
Bensby, T., Feltzing, S., & Oey, M. S. 2014, A&A, 562, A71
Bergemann, M., & Cescutti, G. 2010, A&A, 522, A9
Bergemann, M., & Gehren, T. 2008, A&A, 492, 823
Bergemann, M., Pickering, J. C., & Gehren, T. 2010, MNRAS, 401, 1334
Bielski, A. 1975, JQSRT, 15, 463
Bisterzo, S., Travaglio, C., Gallino, R., Wiescher, M., & Käppeler, F. 2014, ApJ, 787, 10
Borghs, G., de Bisschop, P., van Hove, M., & Silverans, R. E. 1983, HyInt, 15, 177
Bruls, J. H. M. J., Rutten, R. J., & Shchukina, N. G. 1992, A&A, 265, 237
Burris, D. L., Pilachowski, C. A., Armandroff, T. E., et al. 2000, ApJ, 544, 302
Butler, K., & Giddings, J. 1985, Newsletter on the Analysis of Astronomical Spectra, No. 9 (University of London)
Carbon, D. F., Barbuy, B., Kraft, R. P., Friel, E. D., & Suntzeff, N. B. 1987, PASP, 99, 335
Cayrel, R., Depagne, E., Spite, M., et al. 2004, A&A, 416, 1117
Charbonnel, C., & Primas, F. 2005, A&A, 442, 961
Chiappini, C., Matteucci, F., & Gratton, R. 1997, ApJ, 477, 765
Coc, A., Goriely, S., Xu, Y., Saimpert, M., & Vangioni, E. 2012, ApJ, 744, 158
Edvardsson, B., Andersen, J., Gustafsson, B., et al. 1993, A&A, 275, 101
Fabbian, D., Asplund, M., Carlsson, M., & Kiselman, D. 2006, A&A, 458, 899 (F06)
Farouqi, K., Kratz, K.-L., Pfeiffer, B., et al. 2010, ApJ, 712, 1359
François, P., Matteucci, F., Cayrel, R., et al. 2004, A&A, 421, 613
Fu, X., Bressan, A., Molaro, P., & Marigo, P. 2015, MNRAS, 452, 3256
Fuhrmann, K. 2008, MNRAS, 384, 173
Fuhrmann, K. 2011, MNRAS, 414, 2893
Gallagher, A. J., Caffau, E., Bonifacio, P., et al. 2016, arXiv:1605.07215
Gehren, T., Liang, Y. C., Shi, J. R., Zhang, H. W., & Zhao, G. 2004, A&A, 413, 1045
Gehren, T., Shi, J. R., Zhang, H. W., Zhao, G., & Korn, A. J. 2006, A&A, 451, 1065
Goswami, A., & Prantzos, N. 2000, A&A, 359, 191
Gray, D. F. 1977, ApJ, 218, 530
Gustafsson, B., Edvardsson, B., Eriksson, K., et al. 2008, A&A, 486, 951
Ishigaki, M. N., Aoki, W., & Chiba, M. 2013, ApJ, 771, 67
Karakas, A. I. 2010, MNRAS, 403, 1413
Kobayashi, C., Izutani, N., Karakas, A. I., et al. 2011a, ApJL, 739, L57
Kobayashi, C., Karakas, A. I., & Umeda, H. 2011b, MNRAS, 414, 3231
Kobayashi, C., & Nomoto, K. 2009, ApJ, 707, 1466
Kobayashi, C., Tsujimoto, T., Nomoto, K., Hachisu, I., & Kato, M. 1998, ApJL, 503, L155
Kobayashi, C., Umeda, H., Nomoto, K., Tominaga, N., & Ohkubo, T. 2006, ApJ, 653, 1145 (K06)
Korn, A. J., Grundahl, F., Richard, O., et al. 2006, Natur, 442, 657
Kratz, K.-L., Farouqi, K., Pfeiffer, B., et al. 2007, ApJ, 662, 39
Kroupa, P. 2001, MNRAS, 322, 231
Kurucz, R. L., Furenlid, I., Brault, J., & Testerman, L. 1984, Solar Flux Atlas from 296 to 1300 nm (New Mexico: National Solar Observatory)
Lawler, J. E., & Dakin, J. T. 1989, JOSAB, 6, 1457
Lawler, J. E., Wickliffe, M. E., den Hartog, E. A., & Sneden, C. 2001, ApJ, 563, 1075
Lind, K., Asplund, M., & Barklem, P. S. 2009, A&A, 503, 541
Ljung, G., Nilsson, H., Asplund, M., & Johansson, S. 2006, A&A, 456, 1181
Lodders, K., Plame, H., & Gail, H.-P. 2009, in Landolt-Börnstein—Group VI Astronomy and Astrophysics Numerical Data and Functional Relationships in Science and Technology Volume 4B: Solar System, ed. J. E. Trümper (Berlin: Springer)
Maeda, K., & Nomoto, K. 2003, ApJ, 598, 1163
Mashonkina, L. 2013, A&A, 550, A28
Mashonkina, L., Belyaev, A. K., & Shi, J.-R. 2016, AstL, 42, 366
Mashonkina, L., & Gehren, T. 2000, A&A, 364, 249

Mashonkina, L., & Gehren, T. 2001, A&A, 376, 232
Mashonkina, L., Gehren, T., & Bikmaev, I. 1999, A&A, 343, 519
Mashonkina, L., Gehren, T., Shi, J.-R., Korn, A. J., & Grupp, F. 2011, A&A, 528, A87
Mashonkina, L., Gehren, T., Travaglio, C., & Borkova, T. 2003, A&A, 397, 275
Mashonkina, L., Korn, A. J., & Przybilla, N. 2007a, A&A, 461, 261
Mashonkina, L., & Zhao, G. 2006, A&A, 456, 313
Mashonkina, L., Zhao, G., Gehren, T., et al. 2008, A&A, 478, 529
Mashonkina, L. I., Vinogradova, A. B., Ptitsyn, D. A., Khokhlova, V. S., & Chernetsova, T. A. 2007b, ARep, 51, 903
Matteucci, F., & Francois, P. 1989, MNRAS, 239, 885
McWilliam, A., Preston, G. W., Sneden, C., & Shectman, S. 1995, AJ, 109, 2736
Meléndez, M., Bautista, M. A., & Badnell, N. R. 2007, A&A, 469, 1203
Mishenina, T. V., & Kovtyukh, V. V. 2001, A&A, 370, 951
Mishenina, T. V., Pignatari, M., Korotin, S. A., et al. 2013, A&A, 552, A128
Nissen, P. E., & Schuster, W. J. 1997, A&A, 326, 751
Nissen, P. E., & Schuster, W. J. 2010, A&A, 511, L10
Nomoto, K., Kobayashi, C., & Tominaga, N. 2013, ARA&A, 51, 457
Nomoto, K., Tominaga, N., Umeda, H., Kobayashi, C., & Maeda, K. 2006, NuPhA, 777, 424
Pakhomov, Y. V. 2015, ARep, 59, 952
Pakhomov, Y. V., & Zhao, G. 2013, AJ, 146, 97
Pignatari, M., Gallino, R., Heil, M., et al. 2010, ApJ, 710, 1557
Prochaska, J. X., Naumov, S. O., Carney, B. W., McWilliam, A., & Wolfe, A. M. 2000, AJ, 120, 2513
Ralchenko, Y. A., Kramida, E., Reader, J. & NIST ASD Team 2010, NIST Atomic Spectra Database (version 5.4) (Gaithersburg, MD: National Institute of Standards and Technology)
Ramírez, I., Fish, J. R., Lambert, D. L., & Allende Prieto, C. 2012, ApJ, 756, 46
Reader, J., Corliss, C. H., Wiese, W. L., & Martin, G. A. 1980, Wavelengths and Transition Probabilities for Atoms and Atomic Ions: Part 1. Wavelengths, Part 2. Transition Probabilities, NSRDS-NBS 68
Reddy, B. E., Tomkin, J., Lambert, D. L., & Allende Prieto, C. 2003, MNRAS, 340, 304
Reetz, J. K. 1991, PhD thesis, Universität München
Romano, D., Karakas, A. I., Tosi, M., & Matteucci, F. 2010, A&A, 522, A32 (R10)
Roškar, R., Debattista, V. P., Quinn, T. R., Stinson, G. S., & Wadsley, J. 2008, ApJL, 684, L79
Ryabchikova, T., Piskunov, N., Kurucz, R. L., et al. 2015, PhyS, 90, 054005
Ryabchikova, T., Piskunov, N., Pakhomov, Y., et al. 2016, MNRAS, 456, 1221
Rybicki, G. B., & Hummer, D. G. 1991, A&A, 245, 171
Rybicki, G. B., & Hummer, D. G. 1992, A&A, 262, 209
Salvadori, S., Schneider, R., & Ferrara, A. 2007, MNRAS, 381, 647

Samland, M. 1998, ApJ, 496, 155
Sansonetti, C. J., Richou, B., Engleman, R., Jr., & Radziemski, L. J. 1995, PhRvA, 52, 2682
Shi, J. R., Gehren, T., Butler, K., Mashonkina, L. I., & Zhao, G. 2008, A&A, 486, 303
Shi, J. R., Gehren, T., Mashonkina, L., & Zhao, G. 2009, A&A, 503, 533
Shi, J. R., Gehren, T., Zeng, J. L., Mashonkina, L., & Zhao, G. 2014, ApJ, 782, 80
Shi, J. R., Gehren, T., Zhang, H. W., Zeng, J. L., & Zhao, G. 2007, A&A, 465, 587
Siqueira-Mello, C., Andrievsky, S. M., Barbuy, B., et al. 2015, A&A, 584, A86
Sitnova, T., Zhao, G., Mashonkina, L., et al. 2015, ApJ, 808, 148
Sitnova, T. M., Mashonkina, L. I., & Ryabchikova, T. A. 2013, AstL, 39, 126
Sitnova, T. M., Mashonkina, L. I., & Ryabchikova, T. A. 2016, MNRAS, 461, 1000
Smith, G. 1981, A&A, 103, 351
Smith, G. 1988, JPhB, 21, 2827
Smith, G., & O'Neill, J. A. 1975, A&A, 38, 1
Smith, G., & Raggett, D. S. J. 1981, JPhB, 14, 4015
Sneden, C., Cowan, J. J., Kobayashi, C., et al. 2016, ApJ, 817, 53
Spergel, D. N., Bean, R., Doré, O., et al. 2007, ApJS, 170, 377
Spite, M., Andrievsky, S. M., Spite, F., et al. 2012, A&A, 541, A143
Spite, M., Caffau, E., Andrievsky, S. M., et al. 2011, A&A, 528, A9
Spite, M., & Spite, F. 1978, A&A, 67, 23
Spite, M., & Spite, F. 1982, Natur, 297, 483
Steenbock, W., & Holweger, H. 1984, A&A, 130, 319
Takeda, Y., Zhao, G., Chen, Y.-Q., Qiu, H.-M., & Takada-Hidai, M. 2002, PASJ, 54, 275
Thielemann, F.-K., Nomoto, K., & Hashimoto, M.-A. 1996, ApJ, 460, 408
Timmes, F. X., Woosley, S. E., & Weaver, T. A. 1995, ApJS, 98, 617
Travaglio, C., Galli, D., Gallino, R., et al. 1999, ApJ, 521, 691
Travaglio, C., Gallino, R., Arnone, E., et al. 2004, ApJ, 601, 864
Velichko, A. B., Mashonkina, L. I., & Nilsson, H. 2010, AstL, 36, 664
Wallerstein, G. 1962, ApJS, 6, 407
Wood, M. P., Lawler, J. E., Sneden, C., & Cowan, J. J. 2013, ApJS, 208, 27
Woosley, S. E., & Weaver, T. A. 1995, ApJS, 101, 181
Yan, H. L., Shi, J. R., Nissen, P. E., & Zhao, G. 2016, A&A, 585, A102
Yan, H. L., Shi, J. R., & Zhao, G. 2015, ApJ, 802, 36
Zhang, H. W., Butler, K., Gehren, T., Shi, J. R., & Zhao, G. 2006a, A&A, 453, 723
Zhang, H. W., Gehren, T., Butler, K., Shi, J. R., & Zhao, G. 2006b, A&A, 457, 645
Zhang, H. W., Gehren, T., & Zhao, G. 2008, A&A, 481, 489
Zhao, G., Butler, K., & Gehren, T. 1998, A&A, 333, 219
Zhao, G., & Gehren, T. 2000, A&A, 362, 1077
Zhao, G., & Magain, P. 1990a, A&A, 238, 242
Zhao, G., & Magain, P. 1990b, A&AS, 86, 85